

# ACCEPTED VERSION

Elliott W. Lewis, Timothy C.W. Lau, Zhiwei Sun, Zeyad T. Alwahabi, Graham J. Nathan  
**The effect of instantaneous particle distributions on the gas-phase temperature in an unsteady particle-laden jet heated with high-flux radiation**  
International Journal of Multiphase Flow, 2022; 153:104106-1-104106-17

© 2022 Elsevier Ltd. All rights reserved.

This manuscript version is made available under the CC-BY-NC-ND 4.0 license  
<http://creativecommons.org/licenses/by-nc-nd/4.0/>

Final publication at: <http://dx.doi.org/10.1016/j.ijmultiphaseflow.2022.104106>

## PERMISSIONS

<https://www.elsevier.com/about/policies/sharing>

Accepted Manuscript

Authors can share their [accepted manuscript](#):

24 Month Embargo

### After the embargo period

- via non-commercial hosting platforms such as their institutional repository
- via commercial sites with which Elsevier has an agreement

In all cases [accepted manuscripts](#) should:

- link to the formal publication via its DOI
- bear a CC-BY-NC-ND license – this is easy to do
- if aggregated with other manuscripts, for example in a repository or other site, be shared in alignment with our [hosting policy](#)
- not be added to or enhanced in any way to appear more like, or to substitute for, the published journal article

**14 August 2024**

<http://hdl.handle.net/2440/135259>

# The effect of instantaneous particle distributions on the gas-phase temperature in an unsteady particle-laden jet heated with high-flux radiation

Elliott W. Lewis<sup>1,3</sup>, Timothy C. W. Lau<sup>1,3,4</sup>, Zhiwei Sun<sup>1,3</sup>,  
Zeyad T. Alwahabi<sup>2,3</sup>, and Graham J. Nathan<sup>1,3</sup>

<sup>1</sup>*School of Mechanical Engineering, University of Adelaide, Australia*

<sup>2</sup>*School of Chemical Engineering and Advanced Materials, University of Adelaide, Australia*

<sup>3</sup>*Centre for Energy Technology, University of Adelaide, Australia*

<sup>4</sup>*UniSA STEM, University of South Australia, Australia*

## Abstract

Detailed simultaneous planar measurements of particle number density and gas-phase temperature were performed in radiatively heated particle-laden flow within the two- and four-way coupling regimes to evaluate the correlation between the local particle loading and temperature for a series of particle diameters, particle volumetric loadings and radiative heating powers. Utilising novel optical measurement and image processing techniques, together with Voronoi analysis, regions of high instantaneous particle number density (i.e., particle clusters) and localised regions of high/low gas-phase temperatures were identified. The results show that the particle loading measured within the identified ‘hot regions’ was more than 1.5 times greater than the mean value for each case, while within the ‘cold regions’ the particle loading was typically less than the mean. Similarly, the temperature around individual particles was found to increase with an increase in the local particle loading, while the variation in local gas temperature in the vicinity of particles increases with a decrease in particle diameter. Furthermore, the temperature around particles within closely spaced ‘clusters’ was found to be greater than that around particles outside of clusters, even for the same local particle loading. The particle distributions were found to closely match a random Poisson distribution,

consistent with the high particle Stokes numbers ( $86 \leq Sk_D \leq 514$ ), and are not affected by the presence of radiative heating, implying that any flow phenomena induced by thermal gradients in the flow are negligible for the conditions investigated here.

## 1 Introduction

Non-isothermal particle-laden flows with strong radiative heat transfer are relevant to a range of processes in industrial systems, including mineral pre-heating [1], in flames with soot formation [2], particulate fuel burners [3] and for the calcination of alumina and limestone [4, 5]. These calcination processes often require temperatures in excess of 1000 °C for efficient operation, with the energy source historically being the combustion of fossil fuels that contribute significantly to global carbon emissions [6]. As such, the equipment required for these processes needs to be redesigned to transition towards a low-carbon future [7, 8]. Energy sources that have been identified to replace, or be used in conjunction with, the existing combustion-based systems include hydrogen, electricity, biomass and concentrated solar [9]. Efficient and cost-effective optimisation of new systems designed to incorporate non-combusting sources requires reliable, predictive models of the particle-laden flow. However, the current models are limited by a lack of understanding of fundamental heat transfer processes within these flows, partially due to complex, non-linear particle-fluid interactions [10, 11]. Additionally, there is currently a lack of high quality, detailed experimental data for model validation. Therefore, the overall objective of this investigation is to provide high quality experimental data to increase the understanding of heat transfer within non-isothermal particle-laden flows and to support the development of reliable numerical design tools.

Radiative heating of particle suspensions has been increasingly utilised in a range of practical systems such as the indirect calcination in a cement plant [12] and in particle-based concentrated solar thermal (CST) receivers [13], which have shown good potential to replace existing combustion reactors in laboratory-scale experiments [14, 15]. The efficiency of the flow in a CST receiver, defined as the proportion of inlet radiation that is absorbed by the particles, has been previously measured to increase with particle number density due to an increase in the total particle cross-sectional area [16]. However, the average outlet particle temperature was found to decrease with an increase in particle loading, because attenuation of the incident radiation by particles decreases the average radiative heating flux with path length through the flow. This non-uniform temperature distribution due to at-

tenuation has also been observed in spatially-resolved measurements, with the gas-phase temperature of a particle-laden jet flow found to be greater on the side closer to the radiative heating source [17]. Additionally, significant variations in the instantaneous gas temperature were observed, with these variations attributed to the non-uniform instantaneous particle distribution. This relationship between local particle loading and temperature has been previously identified and evaluated in a radiatively heated particle-laden flow using single point detectors [18]. Together, these previous studies have demonstrated that the presence of radiation significantly influences the already complex multi-phase dynamics in particle-laden flows. Despite the advancements made by these studies, current understanding of radiatively heated particle-laden flows is limited by the lack of well-resolved data (both spatially and temporally) of the instantaneous distributions of temperature for either phase in well-characterised particle-laden flows with strong thermal gradients (i.e., high heating rates). These data are needed to provide insights into the physical mechanisms that lead to spatial variations in particle loading and temperature, as well as for the development and validation of reliable, predictive numerical models. Therefore, an aim of the present investigation is to meet this need using simultaneous measurements of the gas-phase temperature and particle loading.

The average particle volumetric loading ( $\phi = \dot{V}_p/\dot{V}_f$ , where  $\dot{V}_p$  and  $\dot{V}_f$  are the respective volumetric flow rates of the particles and fluid) is a key parameter in particle-laden flows that significantly influences the particle-fluid dynamics. For flows with  $10^{-6} < \phi < 10^{-3}$ , called the two-way coupling regime, the momentum exchange between the particles and fluid is sufficient for the flow field of the fluid to differ significantly from that of the single-phase flow [19]. With further increasing  $\phi$ , the flow transitions to the four-way coupling regime, in which particle-particle interactions are also important in addition to the particle-fluid momentum exchange. Importantly, the majority of applications utilising particle-laden flows operate for  $\phi > 10^{-4}$ , so that these coupling effects must be considered for relevant characterisation of the flow [2, 14, 16]. Additionally, in these regimes optical effects such as radiation attenuation and multiple scattering become important [17], which leads to challenges in obtaining well-resolved experimental data. These flows with relatively high particle loading are also challenging to model numerically due to the large number of particles that are required to be simulated, leading to the desirability to introduce simplifying assumptions [10]. However, there is a lack of experimental measurements available of ‘densely’ seeded particle-laden flows to verify such assumptions, particularly for systems with strong radiative heating. Therefore, further detailed measurements of the local gas temperatures in a densely loaded particle-laden flow are required

for continued development of more reliable models.

Another key parameter that influences the particle-fluid interactions is the particle Stokes number  $Sk = \tau_p/\tau_f$ , which characterises how closely a particle will follow flow motions of a given scale. Here,  $\tau_p$  is the particle response time and  $\tau_f$  a suitable time scale of the flow. The Stokes number has also been shown to characterise the formation of particle ‘clusters’, which is a term that is used to denote highly localised flow regions in which the particles accumulate [20]. Hence this term should not be confused with aggregates of particles that are physically connected. Particle clustering occurs through two primary mechanisms: 1) from random variations in the particle motion, resulting in particle distributions that are well described by a Poisson distribution, and 2) from aerodynamic interactions with the flow, which is particularly significant for particles with  $Sk \approx 1$  [21, 22]. In flows with sufficiently strong radiative heating, such variations in the particle distribution can lead to thermal gradients in the gas from convection of sufficient magnitude to generate additional flow phenomena such as buoyancy, which can further modify the velocity and temperature of both phases as well as the particle distributions [23, 24]. The strong temperature gradients in the flow arising from the combination of these complex, coupled, non-linear interactions ultimately affect the stability, efficiency and emissions of processes utilising non-isothermal particle-laden flows. However, the effect of these variable particle distributions on the gas-phase temperature field for flows with radiatively heated inertial particles of relatively high Stokes number ( $Sk > 100$ ), such as are commonly used for particle-based CST receivers [25], is yet to be analysed.

The gas-phase temperature is one of the key parameters required for full characterisation of the heat transfer in radiatively heated particle-laden flows. Additionally, data with high spatial and temporal resolution are required to evaluate the instantaneous thermal gradients within the flow. While direct numerical simulation (DNS) offers the potential to provide this data, fully-resolved simulations of densely seeded particle-laden flows under radiatively heated conditions remain prohibitively expensive in terms of computational time [10]. Therefore, further improvement of the current understanding requires well-resolved experimental data of the gas-phase temperature distributions. Laser-based methods are well suited to provide non-intrusive measurements [26], with commonly used planar gas-phase thermometry techniques including Rayleigh scattering [27], coherent anti-Stokes Raman scattering [28] and laser induced fluorescence (LIF) of a flow tracer [29]. Utilisation of these methods in a flow with particles requires separation of the thermometry signal from the scattered laser light, with the latter typically stronger than the thermometry signal by several orders of magnitude [30]. Additionally, un-

certainties in the signal intensity are influenced by attenuation of the probe laser, signal trapping and multiple scattering [31]. To overcome these challenges, the technique of two-colour LIF has previously been used in conditions with strong optical interference [32, 33], including in particle-laden flows [34]. Two-colour LIF thermometry utilises the temperature dependence of the fluorescence emission spectrum from a suitable tracer seeded into the flow. The temperature is determined using the ratio of fluorescence emission intensity measured within two wavelength bands, which are separated using optical filtering [35]. The advantage of this method is that the thermometry signal is optically separated from the laser scattering due to Stokes shift (i.e., the fluorescence is emitted at wavelengths longer than that of the excitation laser). Additionally, provided that the two signals traverse the same optical path through the flow the calculated ratio is independent of spatial variations in the laser power and tracer concentration, which are particularly significant in particle-laden flows because of attenuation of the excitation beam and signal trapping [17, 31]. Hence, two-colour LIF has been chosen as the method to obtain the requisite planar, well-resolved measurements of the gas-phase temperature for the present investigation.

Despite previous measurements identifying highly variable temperature distributions in radiatively heated particle-laden flows due to the non-uniform particle distribution [17, 18, 36], there is still a need for quantitative assessments of the instantaneous temperature distributions. Therefore, the main objective of the present investigation is to meet this need using simultaneous measurements of the instantaneous spatial distributions of both the gas-phase temperature and particle loading. The present study investigates in detail the influence of the local, instantaneous particle distribution on the gas-phase temperature of the radiatively heated flow, following recent work by the authors that focussed on developing the two-colour LIF technique for use in radiatively heated particle-laden flows [36]. More specifically, the present investigation aims to quantify the degree of the spatial temperature variations measured in a well-characterised and radiatively heated, particle-laden flow within the two- and four-way coupling regimes. A further aim of the present study is to assess the correlation between the local particle loading and gas-phase temperature in the flow. Additionally, the present investigation aims to assess the significance of any motions induced by thermal gradients generated following the absorption of high-flux radiation on the spatial distribution of particles in the flow.

## 2 Methodology

The flow consisted of a particle-laden jet issuing from a long round pipe ( $D = 12.6$  mm,  $L = 2100$  mm) into a weak co-flow, generated from a co-annular pipe of diameter 69 mm with the outlet plane positioned 6 mm upstream from that of the jet, as shown in Figure 1. The key flow parameters and particle properties are summarised in Table 1. This flow configuration with  $L/D > 160$  provides a well-characterised particle-laden jet at the outlet [37]. The experimental arrangement and flow conditions investigated in the present study are identical to those documented by Lewis et al. [17] and Lewis et al. [36], so that only a brief description of the experimental arrangement is provided here. Toluene was chosen as the fluorescent tracer for two-colour LIF because it has good sensitivity to temperature and has previously been demonstrated to be accurate in conditions with strong optical interference [32–34]. Nitrogen was employed as the carrier gas for each flow, with both particles and toluene seeded in the jet flow while the annular flow was seeded only with toluene. The pipe jet had a Reynolds number of  $Re_D = \rho_f U_b D / \mu = 3000$ , where  $\rho_f = 1.15$  kg/m<sup>3</sup> is the density of the ambient (unheated) air,  $U_b = 3.6$  m/s is the flow bulk mean velocity and  $\mu = 1.8 \times 10^{-5}$  Ns/m<sup>2</sup> is the dynamic viscosity of the ambient air. The toluene concentration was approximately 0.75% by volume in the jet and approximately 0.25% by volume in the annular flow. A series of distributions of aluminosilicate particles (Carbobeat CP) with median diameters of  $\bar{d}_p = 173, 205, 238$  and  $423$   $\mu$ m were used, with the particle diameter distribution for each of these presented in Figure 2.

The respective Stokes numbers for each  $\bar{d}_p$ , evaluated at the jet exit plane for the large eddy time scale, were  $Sk_D = (\rho_p \bar{d}_p^2 U_b) / (18 \mu D) = 86, 121, 163$  and  $514$ , where  $\rho_p$  is the particle density. The thermal response of the particles, together with the particle Biot number, was calculated based on well-established empirical and analytical equations for a heated sphere. The Biot number is given by  $Bi = h V_p / A_p k_p$ , where  $V_p$  is the particle volume,  $A_p$  is the particle surface area,  $k_p \approx 2$  is a lower bound estimate for the thermal conductivity of the particles [25],  $h = Nu k_f / \bar{d}_p$  is the convective heat transfer co-efficient, and  $k_f$  is the thermal conductivity of the fluid. The Nusselt number for a spherical particle is given by  $Nu = 2 + \left( 0.4 Re_p^{1/2} + 0.06 Re_p^{2/3} \right) Pr^{0.4} (\mu / \mu_s)^{0.4}$ , and the subscript  $s$  indicates the fluid properties estimated at the particle surface. The particle Reynolds number is given by  $Re_p = \rho_s U_{slip} \bar{d}_p / \mu_s$ , where  $U_{slip} \approx 0.7$  m/s is the estimated particle slip velocity [36, 38], and the Prandtl number is given by  $Pr = c_{p,f} \mu_s / k_{f,s}$ , where  $c_{p,f}$  is the specific heat capacity of the fluid. Result-

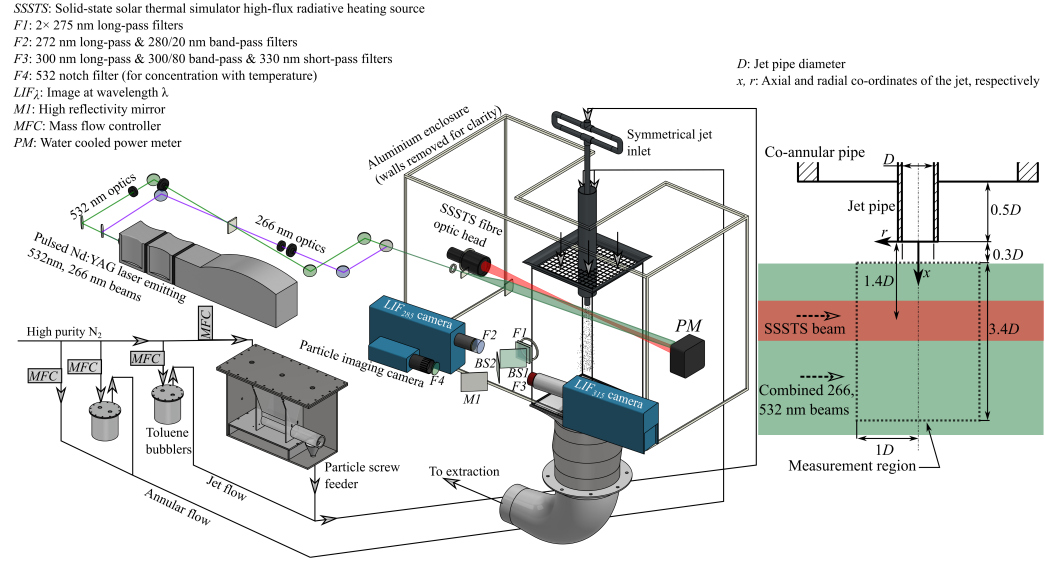


Figure 1: Experimental arrangement for simultaneous planar measurements of the gas-phase temperature, using two-colour LIF, and the particle loading, using laser scattering, in a particle-laden flow heated with high-flux radiation.

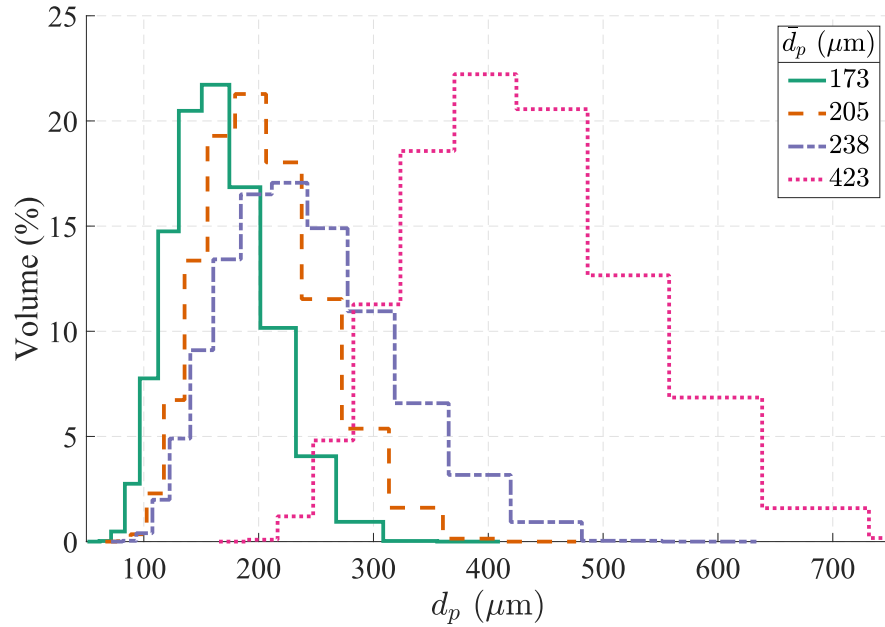


Figure 2: Measured diameter distributions of the particles used in the present investigation.

Table 1: Key parameters used in the present investigation.

Parameter	Symbol	Value	Units
Pipe jet bulk velocity	$U_b$	3.6	m/s
Pipe jet Reynolds number	$Re_D$	3000	-
Annular flow bulk velocity	$U_{a,b}$	0.3	m/s
Particle volumetric loadings	$\bar{\phi} (\times 10^{-3})$	0.625, 1, 1.4	$(\times 10^{-3})$
SSSTS heating powers	$\dot{Q}_0$	0, 910, 1430, 1950, 2410, 2840	W
Particle density	$\rho_p$	3270	kg/m <sup>3</sup>
Particle specific heat	$c_{p,p}(T_p)$	0.7-1.1	kJ/kgK
Particle absorptivity	$\alpha$	0.89	-
Particle emissivity	$\epsilon$	0.85	-
Median particle diameters	$\bar{d}_p$	173, 205, 238, 423	$\mu\text{m}$
Particle Stokes numbers	$Sk_D$	86, 121, 163, 514	-
Estimated Biot number	$Bi$	7.6, 7.8, 8.0, 9.0	-
	$(\times 10^{-3})$		
Estimated thermal time constant	$\tau_p$	6.1, 7.3, 8.5, 15.1	$\mu\text{s}$

antly, the maximum values of the Biot number for the investigated particles was estimated to be  $7.6 \times 10^{-3} < Bi < 9.0 \times 10^{-3}$ . Since  $Bi \ll 1$  the distribution of temperature within the particles are expected to be uniform.

Additionally, the thermal time constant of a radiatively heated spherical particle, given by  $\tau_p = \rho_p c_{p,p} V_p / \dot{Q}'' A_x$ , where  $A_x$  is the particle cross-sectional area, was calculated to be  $6 < \tau_p < 15 \mu\text{s/K}$  for a flux of  $\dot{Q}'' = 42.8 \text{ MW/m}^2$ . Considering that the bulk velocity of the jet was 3.6 m/s, and assuming that convection is negligible, this implies that the particle temperature would increase by 100 °C within the central region of the heating beam (which has a diameter of  $\sim 12 \text{ mm}$ ) in a distance of 2.2 mm for the  $\bar{d}_p = 173 \mu\text{m}$  particles and 5.4 mm for the  $\bar{d}_p = 423 \mu\text{m}$  particles. The time-averaged particle volumetric loadings in the pipe jet used for the present investigation were  $\bar{\phi} = 0.625 \times 10^{-3}$ ,  $1 \times 10^{-3}$  and  $1.4 \times 10^{-3}$ , which result in the jet flows being in the transition region from the two- to four-way coupling regime.

The particle-laden flow was heated using high-flux radiation generated using a solid state solar thermal simulator (SSSTS) that provides a collimated, radially-symmetric, infrared ( $\sim 910 \text{ nm}$ ) beam with a diameter of  $\sim 12 \text{ mm}$  at the focal plane [39]. The SSSTS was operated at a series of output powers

up to  $\dot{Q}_0 = 2840$  W, with a peak radiative flux on the beam axis of approximately  $42.8$  MW/m<sup>2</sup> for this power. The beam was aligned perpendicular to the jet pipe, with the beam axis intersecting the jet centreline  $17.5$  mm downstream from the exit plane as shown by Lewis et al. [17]. The power of the beam transmitted through the flow was monitored during operation using a water-cooled power meter positioned down-beam from the wind tunnel (Gentec model HP100A-4KWHE). The fraction of the beam absorbed by the particles was measured to be up to 19% for the flow with  $\bar{d}_p = 173$   $\mu$ m and  $\bar{\phi} = 1.4 \times 10^{-3}$ , with the absorption found to decrease with a decrease in total particle cross-sectional area (i.e., an increase in  $\bar{d}_p$  and a decrease in  $\bar{\phi}$ ) [36]. The entire region exposed to the heating beam, from the output head to the power meter, was contained within an interlocked aluminium enclosure for safety.

A 266 nm beam from the fourth harmonic of a Nd:YAG laser (Quintel Q-smart), formed into a sheet passing through the jet centreline with a height of 50 mm and thickness 0.6 mm, was used to excite the toluene for two-colour LIF measurements. The second harmonic beam from the same laser (532 nm) was also formed into a sheet co-planar with the 266 nm sheet, with the resultant laser scattering from particles imaged simultaneously with the LIF measurements. The spatially averaged laser pulse fluences for the 266 nm and 532 nm sheets were 50 and 1.4 mJ/cm<sup>2</sup>, respectively.

Optical filters were used to separate the scattered laser light and fluorescence emissions into three channels: two for the two-colour LIF measurements with transmission bands of  $285 \pm 5$  nm and  $315 \pm 10$  nm, respectively, and one to image the scattering from particles at 532 nm. The full details of filters used, together with the transmission bands for the two-colour LIF channels, are presented by Lewis et al. [17]. Each channel shared the same optical path through the flow, so that any attenuation or signal trapping effects were identical for each measurement channel. Two separate PCO Di-Cam intensified sCMOS were used to image the filtered fluorescence channels, using a Sodern Objectif UV 100 F/2.8 lens and a spherical UV lens (Thorlabs LB4821) to image the channels centred at 315 nm and 285 nm, respectively. The spatial resolution of these channels was 17.8 px/mm for  $S_{285}$  and 15.5 px/mm for  $S_{315}$ . A PCO.2000 CCD with a Tamron macro 80-120 mm lens was used to image the laser scattering from particles, with a spatial resolution of 27.3 px/mm. Each camera recorded images simultaneously at the laser pulse frequency of 10 Hz, and had a depth of field estimated to be on the order of centimetres (i.e., greater than the laser sheet thickness).

## 2.1 Image processing

The image processing methods used to determine the gas-phase temperature from the two-colour LIF images and the particle volumetric fraction from the images of laser scattering are described in detail by Lewis et al. [17]. Therefore, only a brief summary of the image processing method is presented here, with typical images to illustrate the key processes being presented in Figure 3. Firstly, background images for all cameras, collected under identical conditions to the main experiment except with the flow switched off, were subtracted from each individual image. Images of a target plate were then used to align each channel to within approximately 1 pixel of each other. The fluorescence images were further aligned to sub-pixel accuracy by minimising the spatial variation in the fluorescence intensity ratio within a region upstream from the heating beam but near the edge of the jet. This region was selected because it has strong gradients in the toluene concentration, so that a slight misalignment between cameras leads to a significant variation in the measured ratio. The pixels from each instantaneous fluorescence image with a signal intensity  $< 15\times$  that of the dark charge were considered to be unreliable and removed from further analysis [34]. The ratio of intensity for each spatially matched pixel was then calculated, from which the temperature was derived using a calibration function. The instantaneous temperature images were then smoothed using a  $5\times 5$  median filter to reduce the influence of noise on the data, which resulted in a net measurement volume of approximately  $0.3 \times 0.3 \times 0.6 \text{ mm}^3$ . The region of interest measured by each camera was bounded by  $0.3 < x/D < 3.7$  and  $|r/D| < 1$ , where  $x$  is the axial direction, parallel to the jet axis, and  $r$  the radial direction, parallel to the laser sheets, with the origin on the jet axis at the outlet plane.

The calibration of intensity ratio to temperature was completed in the same experimental arrangement as for the main experiment, except without particles in the flow and with the central jet pipe heated directly using a controllable electric tape heater. Fluorescence images were recorded at a series of flow temperatures, with the temperature simultaneously measured using a thermocouple inserted into the flow near to the jet exit plane. The resultant best-fit relationship between the intensity ratio and temperature is well-described by a linear function of the form  $S_{315}/S_{285} = 4.50 \times 10^{-3}T_g + 0.98$ , for  $T_g$  in  $^{\circ}\text{C}$  ( $R^2 = 0.9989$ , see also Lewis et al. [17] for more details). It should be noted that this calibration relationship is accurate only for the present experimental arrangement, and not valid broadly, because the relationship is dependent on the filters, optics and cameras used.

For the measurements of laser scattering by particles, a binary mask was generated using a threshold value of  $10\times$  the standard deviation of the

dark charge, to ensure sufficient separation of the scattering from the camera noise. The centres of individual particles were then measured by calculating the intensity centroid. Overlapping particles in each image (i.e., particles at similar locations within the measurement plane but at different depths within the laser sheet) were separated, where possible, using an in-house Matlab code. This was performed by identifying contiguous regions of intensity greater than the threshold that had an area significantly larger than the expected particle area. If this region contained two or more intensity peaks with the intensity distribution surrounding each peak well approximated by a 2D Gaussian distribution, the region was considered to contain multiple particles (corresponding to the number of peaks). The location of the individual particles was then calculated from the location where the Gaussian distribution was at its peak. The particle number density ( $n_p$ ) of each image was then calculated from  $n_p = N_p/V_{532}$ , where  $N_p$  is the total number of particles detected in the image,  $V_{532} = 3.4D \times 1.1D \times (w + d_p)$  is the effective volume from which particles are detected, and  $w = 0.6$  mm is the laser sheet thickness.

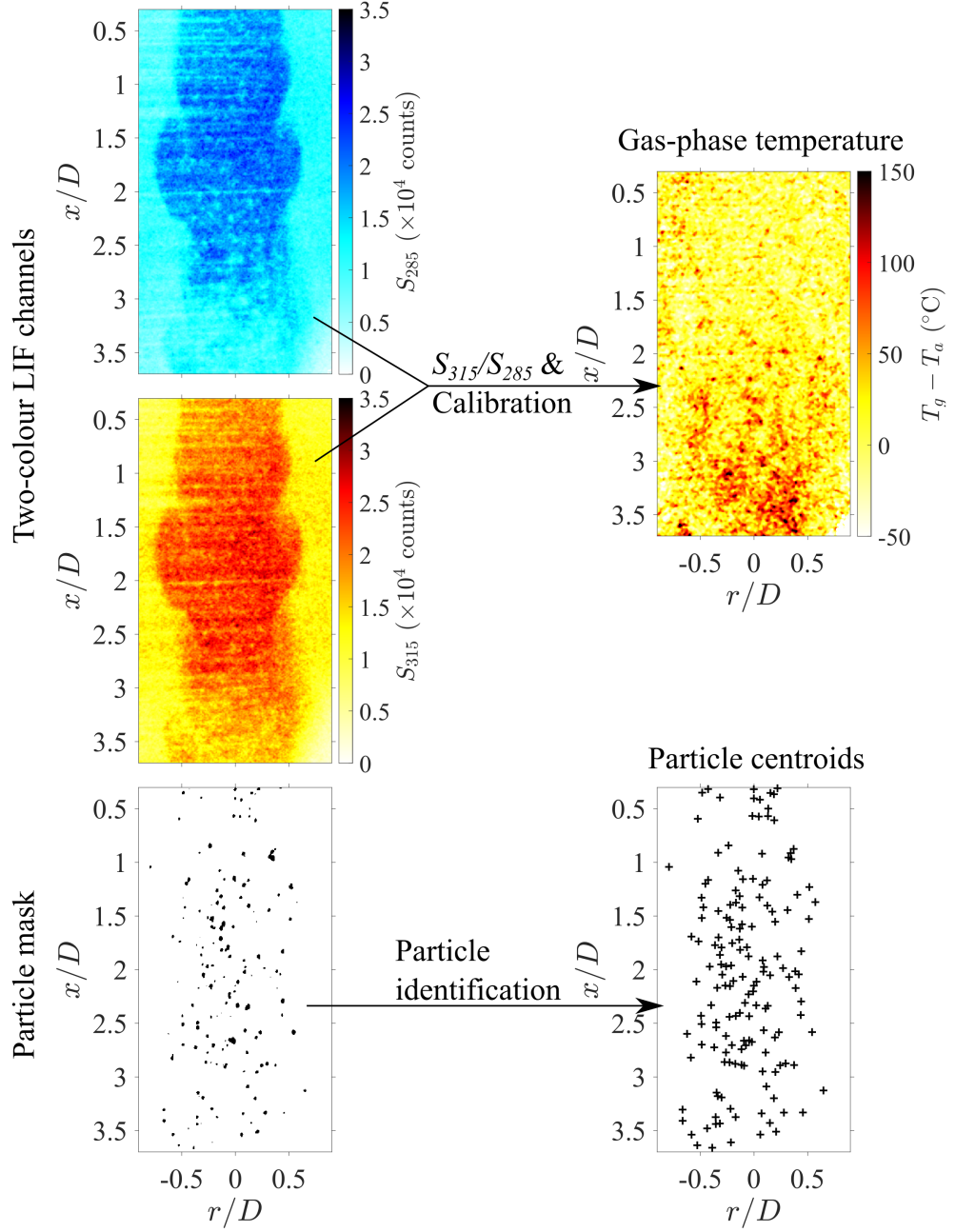


Figure 3: Instantaneous images recorded simultaneously for the two fluorescence channels,  $S_{285}$  and  $S_{315}$ , and the binary mask of particles from the laser scattering channel, following background subtraction and spatial alignment, together with the processed gas-phase temperature distribution and particle centroid locations.

## 2.2 Hot and cold region determination

A new method was developed to determine the regions of the flow where the instantaneous temperature is significantly higher or lower than the average. These are termed ‘hot regions’ and ‘cold regions’, respectively. This method uses quantitative criteria, whose values can be varied systematically, to define the hot and cold regions in a manner that is similar to the method used previously to identify and classify particle clusters [40]. This method is illustrated using a typical instantaneous image for the case with  $Sk_D = 86$ ,  $\bar{\phi} = 1.4 \times 10^{-3}$  and  $\dot{Q}_0 = 2840$  W, as presented in Figure 4. The spatial variations in the instantaneous image of gas-phase temperature above ambient ( $T_g(x, r) - T_a$ ), within and downstream from the heating region ( $0.9 < x/D < 1.9$ ), can be seen in Figure 4a. The variations in the measured temperature are from a combination of the actual spatial variations in the instantaneous gas temperatures and random errors in the measurements. The pixel-to-pixel standard deviation of the unheated flow was measured to be  $17.7$  °C (see also Figure 7a). Although the magnitude of the random errors is typically much smaller than the actual temperature increase measured in the localised hot regions, the pixel-to-pixel random errors result in some pixels registering non-physical values (e.g., regions with  $T_g - T_a < 0$  °C). The hot and cold regions within each individual image were determined from a comparison of the instantaneous temperature distribution with the time-averaged value using the following steps:

1. For the time-averaged temperature image  $\bar{T}_g(x, r) - T_a$ , calculated as the average of  $> 100$  individual images for each flow condition, (Figure 4b), the radially averaged temperature is computed for each row of pixels across the jet over the range  $|r/D| < 0.3$ . This results in a column vector with values corresponding to the jet temperature as a function of distance down-stream from the jet exit. This column vector was then replicated across the width of the original image to form the image  $\bar{T}_{g,CL}(x) - T_a$ , as shown in Figure 4c.
2. The normalised temperature was then calculated for the array using the equation:

$$\Theta(x, r) = \frac{T_g(x, r) - T_a}{\bar{T}_{g,CL}(x) - T_a}, \quad (1)$$

which was evaluated on an element-wise (i.e., pixel-by-pixel) basis. This normalisation was performed using  $\bar{T}_{g,CL}(x)$ , rather than  $\bar{T}_g(x, r)$ , because large errors can occur in regions with  $\bar{T}_g(x, r) \approx 0$ , such as near to the jet edge. Regions with  $\bar{T}_{g,CL}(x) - T_a < 3$  °C (i.e., where the denom-

inator term used to calculate  $\Theta(x, r)$  is close to zero) were considered unreliable and hence were removed from further analysis.

3. Each individual image of  $\Theta(x, r)$  was then smoothed using a circular Gaussian filter kernel  $f$  with a characteristic smoothing length scale  $L_S = 4\sigma$ , where  $\sigma$  is the standard deviation of the Gaussian function, expressed as:

$$f(m, n) = \exp \left[ -8 \left( \frac{m^2 + n^2}{L_S^2} \right) \right], \quad (2)$$

where  $m$  and  $n$  are the array indices in the  $r$  and  $x$  directions with respect to the origin, respectively. Using this, the value of each pixel  $(i, j)$  of the smoothed temperature field  $\Theta_S(x, r)$  is given by:

$$[\Theta_S]_{i,j} = \left( \sum_{m=-\delta}^{\delta} \sum_{n=-\delta}^{\delta} f_{m,n} [\Theta]_{i-m,j-n} \right) \times \left( \sum_{m=-\delta}^{\delta} \sum_{n=-\delta}^{\delta} f_{m,n} \right)^{-1}, \quad (3)$$

where  $\delta = L_S/2$  is chosen for the bounds of the smoothing kernel size. Figure 4d presents the instantaneous, normalised temperature after smoothing with  $L_S = 0.1D$ .

4. For each individual image, the reference temperature difference,  $\Theta_{ref}$ , was calculated as the spatial average of  $\Theta(x, r)$  in the region of  $2.5 < x/D < 3$  and  $|r/D| < 0.25$ . The hot and cold regions were then identified as regions with  $\Theta_S(x, r)$  that differed significantly from this reference. Threshold values were used to separate the hot and cold regions, with the thresholds for the hot and cold regions,  $\epsilon_H$  and  $\epsilon_C$ , respectively, calculated as a function of axial distance from the equations:

$$\epsilon_H(x, L_S) = \Theta_{ref} + \frac{k\sigma_T(x, L_S)}{\bar{T}_{g,CL}(x) - T_a} \quad (4)$$

and

$$\epsilon_C(x, L_S) = \Theta_{ref} - \frac{k\sigma_T(x, L_S)}{\bar{T}_{g,CL}(x) - T_a}, \quad (5)$$

where  $\sigma_T(x, L_S)$  is the axial profile of the pixel-to-pixel standard deviation of  $\Theta_S(x, r)$ , calculated from all pixels with  $|r/D| < 0.3$ . The symbol  $k$  represents a multiplier to the standard deviation. The threshold profile calculated for the example image with  $L_S = 0.1D$  and  $k = 1$  is presented in Figure 4e. The resultant hot and cold regions, overlaid on the image of  $\Theta_S(x, r)$ , are presented in Figure 4f.

5. The hot/cold regions with an area less than  $0.008D^2$  (corresponding to the area of a circle with diameter  $0.1D$ ) were considered to be too small for reliable measurement and thus removed from further analysis.

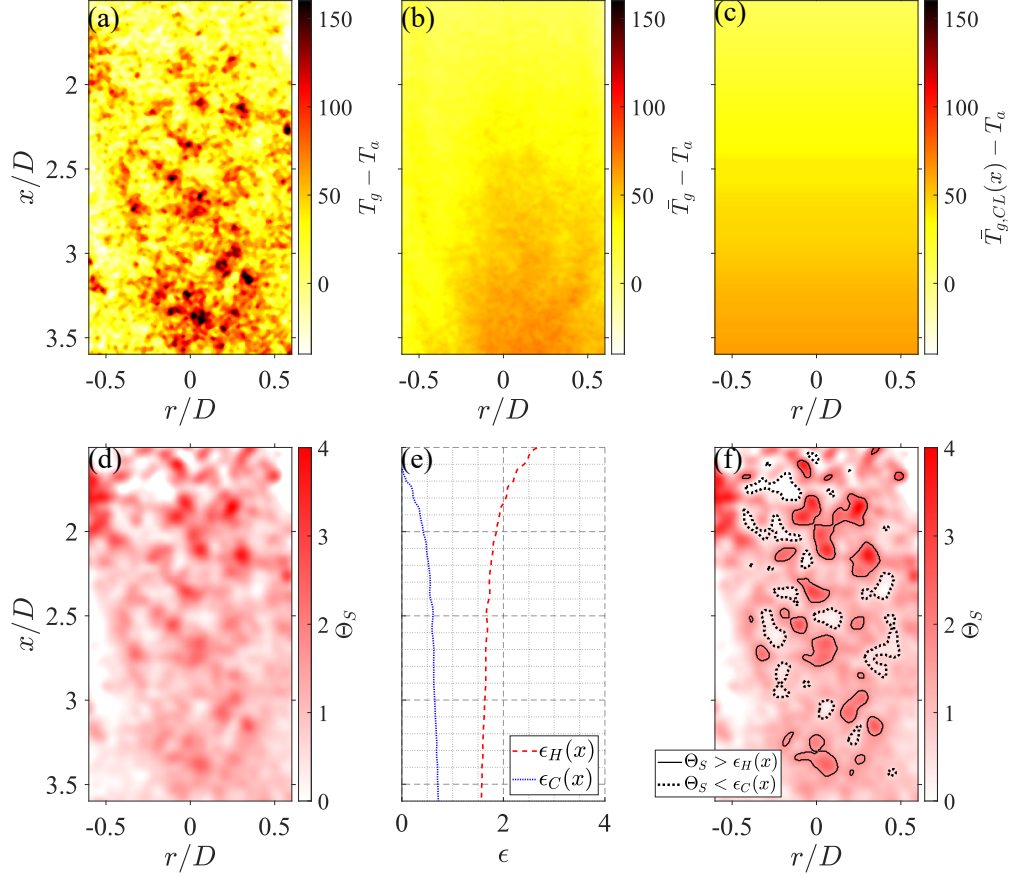


Figure 4: The method used to determine local areas of relative high and low temperature: (a) a typical instantaneous gas-phase temperature image,  $T_g - T_a$ , (b) the time-averaged temperature image,  $\bar{T}_g - T_a$ , (c) the axial profile of the time- and radially-averaged temperature in the region  $|r/D| < 0.3$  after replication into an array across the width of the original image,  $\bar{T}_{g,CL}(x) - T_a$ , (d) the smoothed normalised temperature increase from ambient,  $\Theta_S$ , (e) the thresholds used to determine hot and cold regions,  $\epsilon_H(x)$  and  $\epsilon_C(x)$ , respectively, and (f)  $\Theta_S$  together with the boundaries of the determined hot and cold regions.

## 2.3 Particle cluster determination

Flow regions with a relatively high local particle volumetric fraction (clusters), and those with no nearby particles (voids), were determined from the images of laser scattering using the well-established Voronoi method [22]. An example of the processed laser scattering image is presented in Figure 5a. The Voronoi method involves partitioning the image into cells around each particle centroid, with the region belonging to each cell comprised of the ensemble of locations that are closer to the associated particle than any other. The co-ordinates of the vertices around each cell were used to calculate the area of each individual Voronoi cell,  $A_{cell}$ . Cells with vertices outside of the measurement region, such as for particles near to the jet edge, were removed from further analysis. The Voronoi diagram for the example image is presented in Figure 5b.

In the present investigation, particles were defined to be within clusters if two or more adjacent Voronoi cells met the condition:

$$A_{cell}(x) < e_p \bar{A}_{cell}(x) \quad (6)$$

where  $e_p$  is a threshold value and  $\bar{A}_{cell}$  is the median area of the Voronoi cells, calculated as a function of axial location. A value of  $e_p = 0.706$  was chosen for the threshold because this results in 1/3 of all Voronoi cells of a Poisson distribution having an area below the threshold [41]. This constant threshold value was chosen, rather than using an adaptive threshold such as presented by Monchaux et al. [22], because the adaptive threshold method requires the probability density function (PDF) of the cell areas to be calculated. The latter method was considered to be unreliable for the cases with low particle number density investigated here. A constant threshold for cluster determination was also used in the previous cluster analysis performed by Lau et al. [42]. The Voronoi cells that were considered to be clusters are also shown in Figure 5b with blue shading.

Using these definitions, both the gas-phase temperature and local particle volumetric fraction were calculated within regions of the following size:

1.  $< 0.1D$  from the centroid of particles within clusters ( $T_{g,Hi}$ );
2.  $< 0.1D$  from particles that are outside of clusters ( $T_{g,Lo}$ ), and;
3. void regions ( $T_{g,Vd}$ ).

For the present investigation the voids were defined as regions that are further than  $0.1D$  from the nearest particle, to match the length scale chosen to identify the hot and cold regions (Section 2.2). The void regions of the

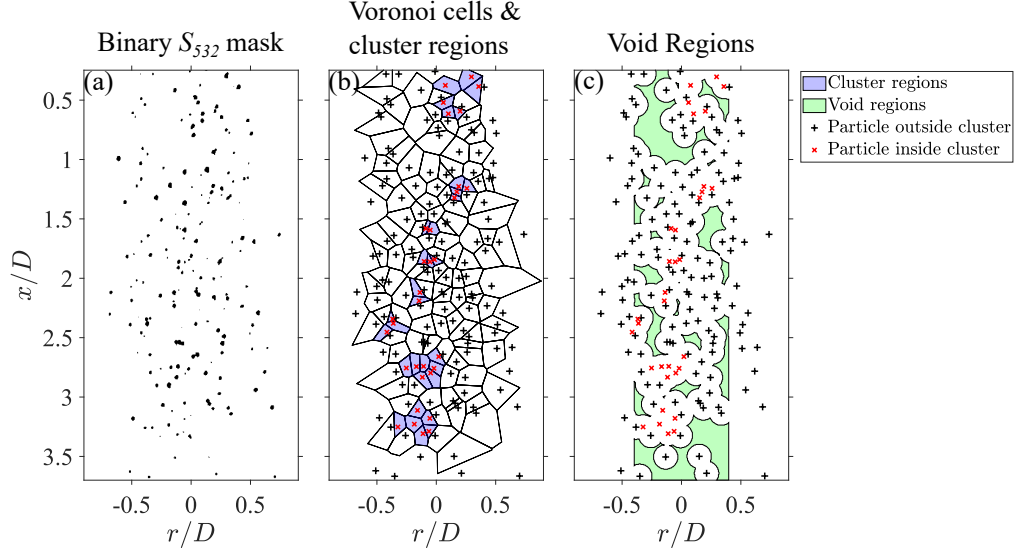


Figure 5: The binary particle mask from  $S_{532}$  (a), the resultant particle centroids together with the calculated Voronoi cells and determined clusters (b), and the void locations (c) for a single image from the case with  $\bar{d}_p = 173 \mu\text{m}$  and  $\phi = 1.4 \times 10^{-3}$ .

example image are presented in Figure 5c, together with the locations of particles both inside and outside of clusters. The calculation of the voids was limited to regions with  $|r/D| < 0.4$ , to avoid bias towards the jet edge regions with a low particle number density and low average local temperature rise. It should be noted that regions where  $T_{g,Hi}$  and  $T_{g,Lo}$  are measured can overlap for the case where two particles, one of which is considered to be inside of a cluster and the other not, have centroids that are less than a distance  $0.2D$  from each other.

## 2.4 Random particle simulation

A simulation of a random distribution of particles was also performed for each combination of  $\bar{d}_p$  and  $\bar{\phi}$  employed in the experiment, to assess how closely the random and measured distributions match. This method to simulate the particle distribution is identical to that presented by Lewis et al. [36], so that only a brief summary is presented here. Particle positions were generated randomly in a cylindrical spatial domain with both a length and diameter of  $1.5D$  such that the resultant average radial distribution matched previous measurements under identical conditions to the present experiments [17]. In the simulation, only those particles that were located within a volume

corresponding to that of the laser sheet were retained. The particles within this simulated laser sheet were then analysed using the same Voronoi method as was used for the experiments. The results of the cluster analysis for the simulated results were compared with the experimental measurements.

### 3 Results

#### 3.1 Hot and cold region detection sensitivity

The top sub-figure of Figure 6 presents the number of hot and cold regions in the flow that were measured to be larger than the cut-off area of  $0.008D^2$  ( $N_{reg}$ ) normalised by the peak value ( $N_{reg,max}$ ), as a function of  $L_s$  for the series of  $Sk_D$  investigated in this study. This assesses the sensitivity of the smoothing length scale used in equations 2 and 3,  $L_s$ . In this figure, the average particle volumetric loading was  $\bar{\phi} = 1.4 \times 10^{-3}$  and the heating beam power was  $\dot{Q}_0 = 2840$  W. The results show that, in general,  $N_{reg}/N_{reg,max}$  increases with an increase in  $L_s$  for  $L_s < 0.075D$  and decreases with an increase in  $L_s$  for  $L_s > 0.1D$ . The peak of  $N_{reg}/N_{reg,max}$  occurs for values of  $0.075D < L_s < 0.1D$  for each case, which agrees well with what can be visually seen in the instantaneous temperature image (see Figure 4). For these reasons, a smoothing length scale of  $L_s = 0.1D$  was used for the present investigation.

The bottom sub-figure of Figure 6 presents the average value of the normalised, smoothed temperature obtained using equations 1-3 within the hot and cold regions ( $\Theta_{reg}$ ) as a function of the standard deviation multiplier used to calculate the threshold in equations 4 and 5,  $k$ . The difference between the time-averaged normalised temperature of the flow (i.e.,  $\Theta = 1$ ) and the temperature within the detected hot and cold regions can be seen to increase with an increase in  $k$ , which is consistent with the threshold values calculated using equations 4 and 5. However, it can be seen that the value of  $\Theta_{reg}$  is only weakly dependent on  $k$ . Because of this, the commonly used statistical value of one standard deviation from the mean (i.e.,  $k = 1$ ) was used for the threshold calculations in the present investigation.

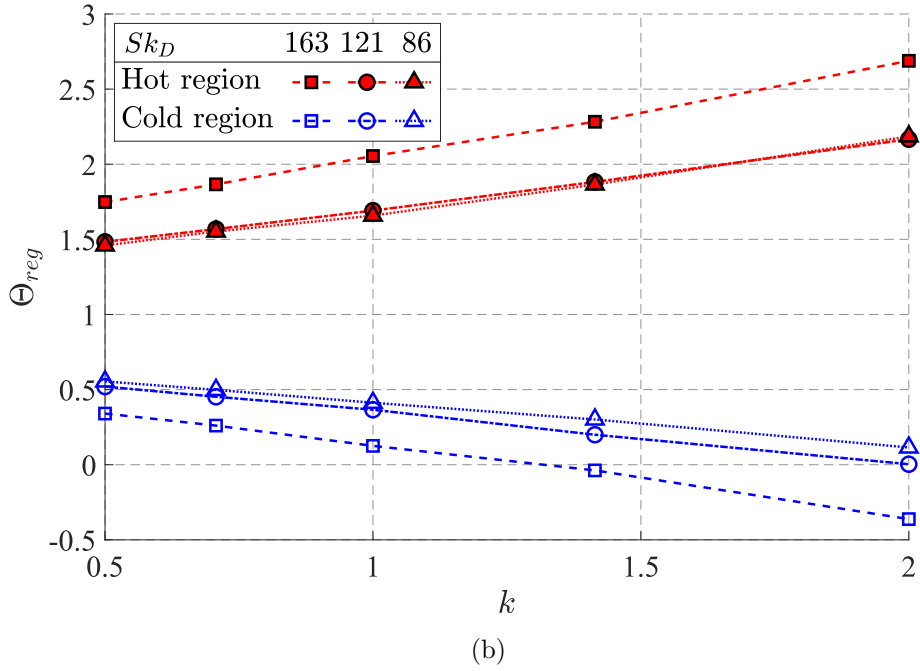
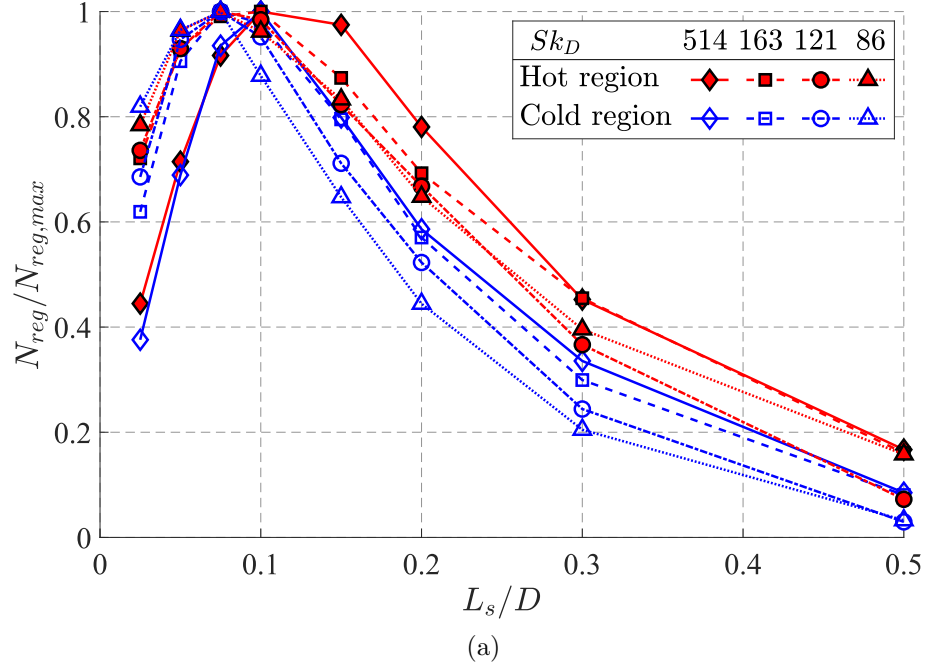


Figure 6: The number of hot and cold regions ( $N_{reg}$ ) normalised by the peak value as a function of smoothing length scale (a), together with the normalised temperature measured in these regions ( $\Theta_{reg}$ ) as a function of the threshold multiplier,  $k$ , (b) for the series of Stokes numbers investigated. The  $Sk_D = 514$  case is not presented in the bottom sub-figure because the temperature increase is insufficient for reliable calculation of  $\Theta_{reg}$ .

### 3.2 Temperature and particle volume fraction measurements

Figure 7 presents probability density functions (PDF) of both the measured gas-phase temperature above ambient,  $T_g - T_a$ , (a) and the smoothed normalised temperature,  $\Theta_S$ , (b) for a series of axial locations for the case with  $Sk_D = 86$ ,  $\bar{\phi} = 1.4 \times 10^{-3}$  and  $\dot{Q}_0 = 2410$  W. The PDFs at each location were calculated from the ensemble of all pixels, from all relevant images, that are within an axial range of  $\pm 0.125D$  about the specified location and within a radial range of  $|r/D| < 0.5$ . The inset for (a) presents the normalised PDF of  $T_g - T_{g,M}$ , where  $T_{g,M}$  is the modal value of the PDF, while the inset for (b) presents the PDF of  $\Theta_S$  on a log scale, to better show the tails of the PDF. The shape of the PDF at  $x/D = 0.75$  (i.e., upstream from the heating region) is well approximated by a Gaussian curve centred at  $T_g - T_a = 0$  °C, with a standard deviation in the measurements of  $\sigma_{TG} = 17.7$  °C. This can be seen from comparison with the Gaussian curve with this standard deviation, presented in the inset. The measured temperature variation at  $x/D = 0.75$  is not physical, but is due instead to the random errors in the measurement. This standard deviation is consistent with the pixel-to-pixel value of 16.8 °C that was previously determined for the measurement of the unheated jet flow [17]. The results also show that the peak (modal value) of the PDFs increases with axial distance, with the peak for  $x/D = 2, 2.75$  and  $3.5$  at temperatures of  $T_g - T_a = 12.5, 22.5$  and  $33.5$  °C, respectively. This is consistent with the measured increase in the time-averaged temperature [36], of  $\bar{T}_g - T_a = 17.3, 31.2$  and  $42.6$  °C, respectively. Additionally, the range of temperatures that were measured in the flow increases with axial distance, with the standard deviation of the PDFs of  $T_g - T_a$  increasing from  $\sigma_{TG} = 23.0$  °C at  $x/D = 2$  to  $\sigma_{TG} = 36.0$  °C at  $x/D = 3.5$ . The shape of the PDF of  $T_g - T_a$  also becomes positively skewed downstream from the heating region. That is, the proportion of the flow with a temperature higher than the peak (modal) value increases with axial distance downstream from the beginning of the heating region at  $x/D = 0.9$ . This can be seen at  $x/D = 2.75$ , for which the modal temperature measured was  $T_g - T_a = 22.5$  °C with measurements in the range  $-40$  °C  $< T_g - T_a < 170$  °C.

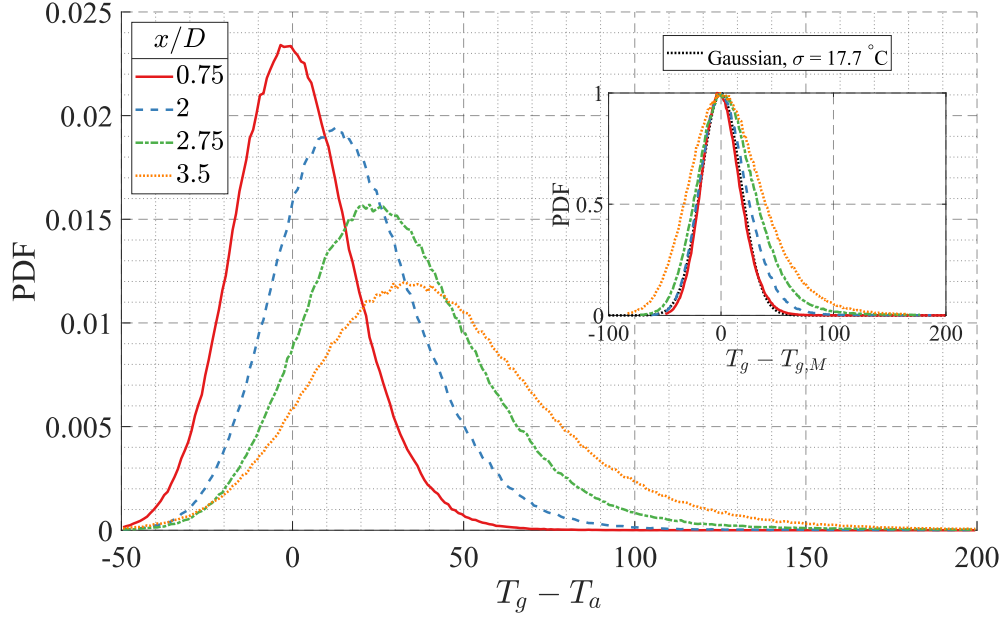
The PDFs of the normalised and smoothed temperature  $\Theta_S$  collapse closely for  $x/D \geq 2.75$ , with the shape approaching a skewed Gaussian distribution with a modal value of  $\Theta_S = 0.80$ . The collapse of the PDFs implies that the relative spread of temperatures measured remains consistent with axial distance from the end of the heating region. For the axial location of  $x/D = 2$ , the PDF profile has a greater range of values and a lower modal value of  $\Theta_S = 0.77$  compared to the downstream locations. The

greater variation that can be seen for the measurements at this axial location is attributed to the measurement uncertainty being more significant in the calculation of  $\Theta_S$  for relatively low  $T_g - T_a$  (i.e., regions with little convective heating). The proportion of the flow with  $\Theta_S < \epsilon_C$  (i.e., the cumulative sum of the PDF to the left of the vertical line denoting  $\epsilon_C$ ) for the typical flow, such as at  $x/D = 2.75$ , was 14.2%, while  $\Theta_S > \epsilon_H$  in 9.9% of the flow. This means that there are expected to be more cold regions than hot regions, most likely due to the influence of the flow areas with a low average particle volume fraction near to the jet edge.

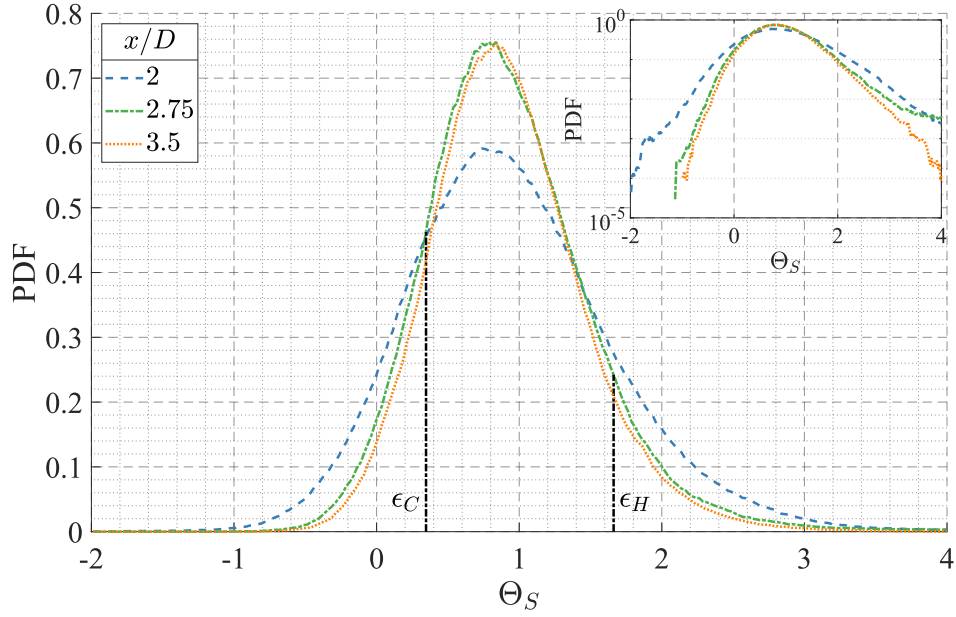
Figure 8 presents the number of particles within clusters from each relevant image normalised by the total number of particles detected,  $N_{p,clus}/N_p$ , as a function of  $\dot{Q}_0$  for a constant value of  $\bar{\phi} = 1.4 \times 10^{-3}$  for the series of particle Stokes numbers/particle number densities investigated (top) and  $N_{p,clus}/N_p$  as a function of  $n_p$  for each combination of  $Sk_D$  and  $\bar{\phi}$  (bottom). Also included in the bottom sub-figure is the values of  $N_{p,clus}/N_p$  calculated from the simulation of a random particle distribution described in Section 2.4. These results are from the region bounded by  $1.5 < x/D < 2.5$  and  $|r/D| < 0.3$ , in which the time-averaged particle number density is close to uniform [17]. Note that this region contains the flow both within, and immediately downstream from, the heating beam.

The measured proportion of particles in clusters  $N_{p,clus}/N_p$  increases with a decrease in particle Stokes number (i.e., an increase in particle number density), with up to 23% of particles being identified as part of clusters for the flow with  $Sk_D = 86$  ( $n_p = 0.39$  particles/mm<sup>3</sup>). The proportion of the flow detected to be in clusters for the case with  $Sk_D = 514$  is approximately half of that for  $Sk_D \leq 163$ . This is predominantly attributed to the reduction in particle number density with an increase in  $Sk_D$  rather than to any direct role of the Stokes number, since  $Sk_D \gg 1$  for all cases. The particle number density is proportional to  $1/\bar{d}_p^3$ , such that the number of particles detected in the analysed region of each image, for the constant loading of  $\bar{\phi} = 1.4 \times 10^{-3}$ , decreases from  $n_p = 0.39$  particles/mm<sup>3</sup> for  $Sk_D = 86$  to  $N_p = 0.04$  particles/mm<sup>3</sup> for  $Sk_D = 514$ . This decrease in number density means that the proportion of particles that are removed from the Voronoi analysis due to having an infinite cell area increases (e.g., those near to the jet edge), resulting in fewer valid cells for the cluster analysis.

No trends are evident in  $N_{p,clus}/N_p$  as a function of heating power for any of the particle diameter distributions investigated. This implies that particle clustering is not affected by any flow phenomena driven by thermal gradients, including buoyant plumes, thermophoresis, turbulence generation or particle migration. That is, the particle momentum/inertia dominates over any forces induced by thermal gradients within the near-field of the jet ( $x/D < 3.7$ ).



(a)



(b)

Figure 7: Probability density function of the measured gas temperature for the case with  $Sk_D = 86$ ,  $\bar{\phi} = 1.4 \times 10^{-3}$  and  $\dot{Q}_0 = 2410$  W before (a) and after (b) normalisation and smoothing, for a series of axial locations. The ensemble of data used for each profile was from pixels in all images with  $r/D < 0.5$  and within  $0.125D$  axially of the displayed value. The vertical lines represent typical threshold values used to determine hot and cold regions,  $\epsilon_H$  and  $\epsilon_C$ , respectively. The inset of (a) presents compares the measured PDFs of temperature to a Gaussian curve, while the inset of (b) presents the PDF of  $\Theta_S$  with the y-axis on a log-scale.

However, this is not to say that the influence of radiative heating on the gas-phase is insignificant, or that the particle number density and velocity distributions further downstream are unaffected.

The proportion of particles measured to be in clusters can be seen to increase with  $n_p$  within the region bounded for these measurements, with the measured results closely matching those of the simulation. This suggests that the spatial variations in the particle distribution that lead to the detected clusters are primarily driven by random fluctuations rather than aerodynamic effects. This is consistent with previous studies that have shown that aerodynamic clustering is only significant for  $Sk \sim O(1)$  [21, 22], while in the present measurements the Stokes number is  $Sk_D \geq 86$ . It should be noted that, while  $Sk_D$  is also dependent on the flow temperature through gas viscosity, it is expected to decrease by less than 27% in the range  $0 \leq T_g - T_a \leq 150$  °C. Hence, although the clustering in these high-Stokes number flows is not as prevalent as for flows with  $Sk \sim O(1)$ , the random variations still result in sufficient spatial and temporal variations in the particle volume fraction to generate complex and non-uniform heat transfer processes in the flow.

Figure 9 presents typical instantaneous images of the temperature above ambient,  $T_g - T_a$ , (top), the normalised temperature smoothed using a length scale of  $L_S = 0.1D$ ,  $\Theta_S$ , together with the boundaries of the hot and cold regions (middle) and the locations of particles that have been determined to be either within or outside of clusters (bottom), for each  $Sk_D$  with  $\phi = 1.4 \times 10^{-3}$  and  $\dot{Q}_0 = 2840$  W. The hatched regions in the image correspond to the cases of  $\Theta_S$  that were removed from the analysis due to having a temperature rise  $\bar{T}_{g,CL} - T_a < 3$  °C. The regions for which  $\bar{T}_{g,CL} - T_a > 3$  °C include those with  $x/D \geq 1.5$  for the cases with  $Sk_D \leq 163$  and  $x/D > 2.3$  for  $Sk_D = 514$ . It can be seen that a decrease in  $Sk_D$  increases the area of the hot and cold regions, particularly for  $x/D > 2$ . For each  $Sk_D$  the hot and cold regions boundaries typically exhibit an of irregular, ellipse-like shape whose primary axes are aligned at an angle of approximately 45 ° to the jet axis. This shares some similarity with the oblique angles seen of clusters in a particle-laden jet, for particles with  $Sk_D \approx 1.4$  and is consistent with a role of large-scale, shear-driven vortical motions [40]. The detected hot regions can be seen to be more prevalent on the jet axis than near to the edge, while the cold regions are more common near to the jet edge. This is consistent with both the particles being preferentially concentrated towards the jet centreline [17] and with the entrainment of cold flow through convection/mixing with the unheated co-flow being greatest at the jet edge.

The decrease in particle number density with an increase in  $Sk_D$  for constant  $\bar{\phi}$  can be seen from the number of particles imaged for each case, with the resultant proportion of the gas that is within the void regions increasing

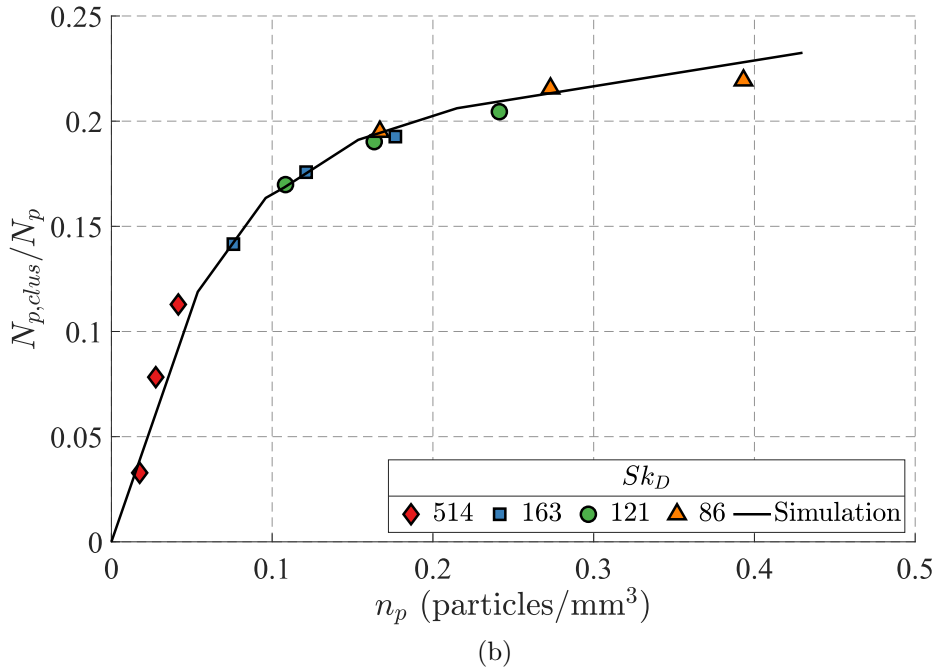
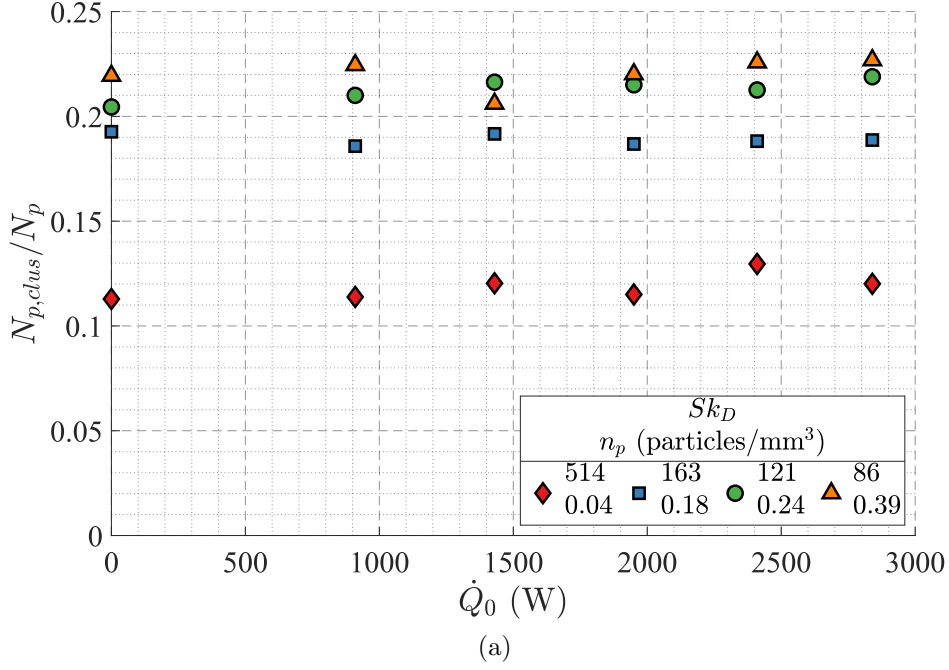


Figure 8: The measured number of particles determined to be in a cluster ( $N_{p,clus}$ ) normalised by the total number of particles ( $N_p$ ), in the region  $1.5 < x/D < 2.5$  and  $|r/D| < 0.3$ , as a function of the heating beam power with a constant value of  $\bar{\phi} = 1.4 \times 10^{-3}$  for a series of particle number densities (a) and  $N_{p,clus}/N_p$  as a function of the particle number density  $n_p$  for each combination of  $Sk_D$  and  $\phi$  (markers), together with the results from the random particle distribution simulation (line).

significantly with  $Sk_D$  from 24% for  $Sk_D = 86$  to 79% for  $Sk_D = 514$ . The location of the hot regions shows good qualitative agreement with regions of high local particle volume fraction, particularly for the case with  $Sk_D = 86$ . Heat transfer between the gas in the measurement region and particles outside of, but near to, the diagnostic laser sheet also influences the measured gas-phase temperature, such that heated regions can also appear where no particles were imaged. However, the influence of these particles on the measured temperature is expected to be less than that of the particles imaged within the laser sheet because of the greater distance between the particle and measurement regions.

Figure 10 presents a series of four consecutive images of  $T_g - T_a$ , together with the corresponding image of  $\Theta_S$ , for the flow with  $Sk_D = 86$ ,  $\bar{\phi} = 1.4 \times 10^{-3}$  and  $\dot{Q}_0 = 2840$  W. The detected boundaries of the hot and cold regions, together with the particle locations, are superimposed on the images of  $\Theta_S$  to graphically show the correlation between the local particle volume fraction and gas temperature. In the region downstream from the heating beam, for  $x/D > 1.9$ , the temperature can be seen to vary spatially and temporally (i.e., from image to image) by up to  $\sim 150$  °C, even at similar axial locations. The basic trends identified from the temperature distributions presented in Figure 9 can also be seen in each image here, with the flow exhibiting localised regions of high and low temperature relative to the surroundings. No clear structure can be seen from these temperature variations, with the location, size and shape of the hot and cold regions being irregular. The superimposed particle locations more clearly show the correlation between  $\Theta_S$  and the particle locations, with the hot regions tending to contain several particles while few particles are detected within the cold regions. These trends are consistent for all combinations of  $Sk_D$  and  $\bar{\phi}$  with  $\dot{Q}_0 > 0$  investigated, but are most clearly demonstrated for the presented case (which has the greatest average temperature increase among all investigated cases). The framing rate of the current measurements is too slow compared with the flow time-scales to assess any coherence between successive frames. Nevertheless, the planar measurements do provide evidence of coherence, because the locations of particles strongly correspond to locations where the gas temperature rise is high at all axial locations downstream from the heating region. This suggests that, within the first few diameters from the exit plane, the particles and fluid surrounding the particles travel coherently with little transport to the bulk flow.

To provide further evidence of the correlation between the particle locations and gas temperature, the instantaneous particle volume fraction within the boundaries of each hot and cold region,  $\phi_{reg}$ , was calculated. The value of  $\phi_{reg}$  was then normalised by the time-averaged volume fraction evaluated

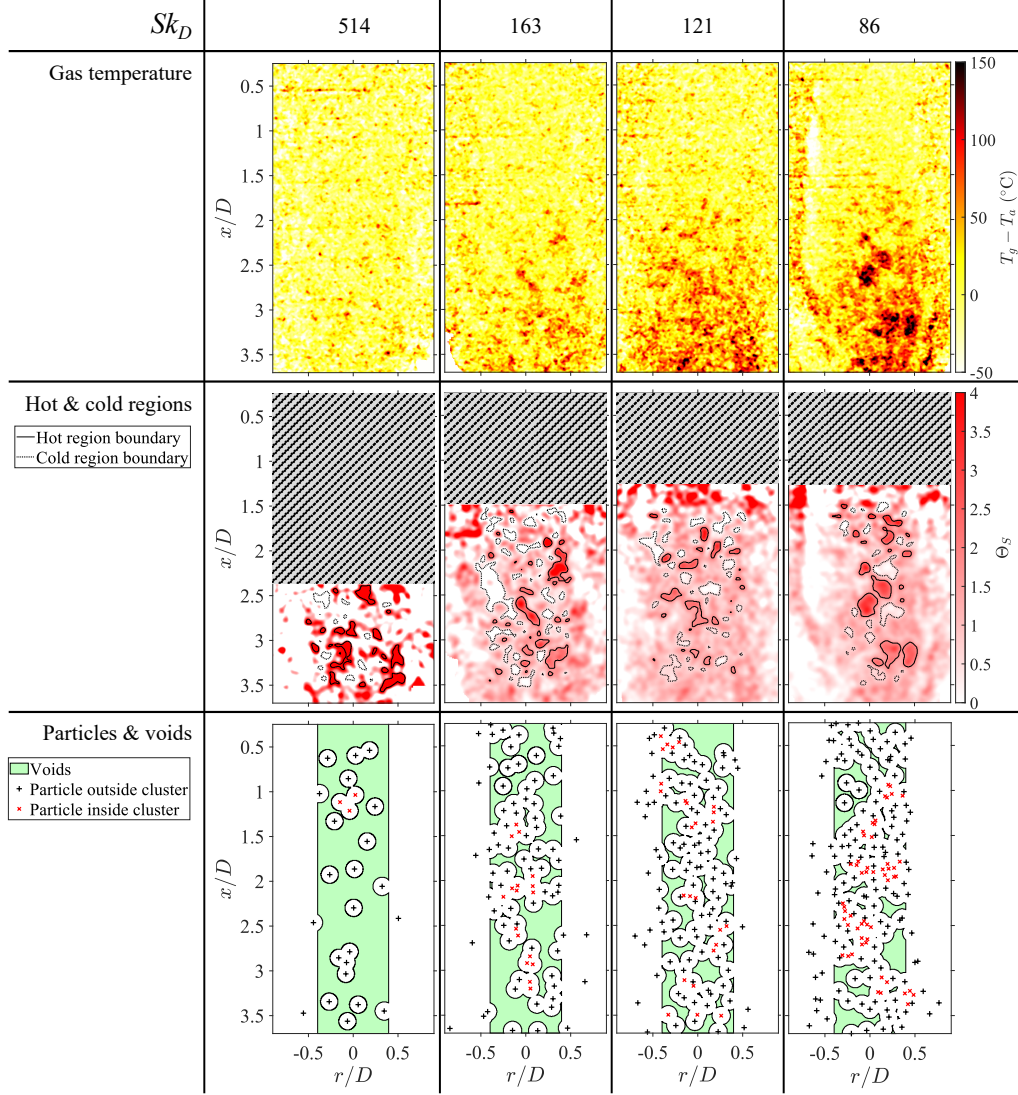


Figure 9: Typical instantaneous images of the temperature above ambient (top), the normalised and smoothed temperature  $\Theta_S$  together with the boundaries of the determined hot and cold regions (middle), and the particle locations together with the determined void regions (bottom), for each flow Stokes number  $Sk_D$ . For each image presented the particle volumetric loading was  $\phi = 1.4 \times 10^{-3}$  and the heating beam power was  $\dot{Q}_0 = 2840$  W. The hatched regions denote areas with an insufficient temperature rise for reliable calculation of  $\Theta_S$ .

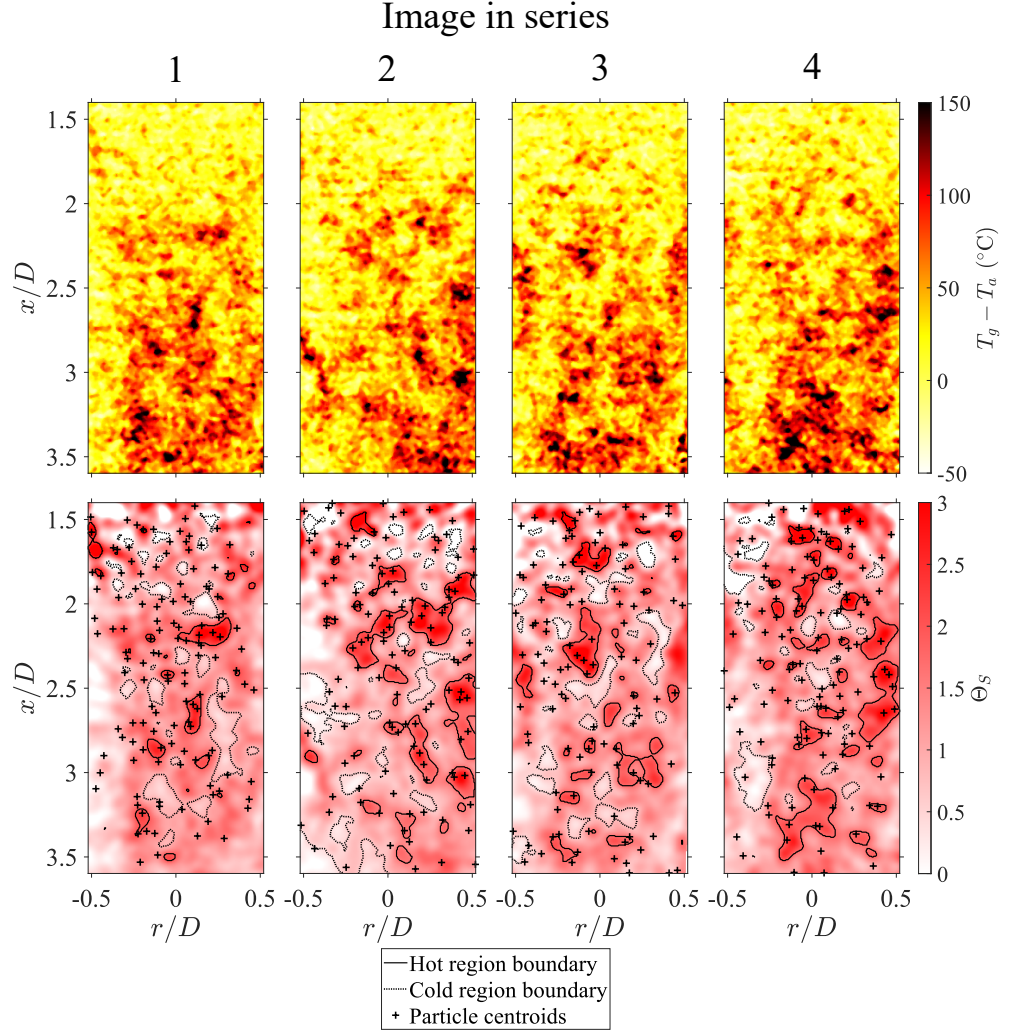


Figure 10: A series of consecutive images of the temperature, together with  $\Theta_S$ , for the flow with  $Sk_D = 86$ ,  $\phi = 1.4 \times 10^{-3}$  and  $\dot{Q}_0 = 2840$  W. The particle centroid locations and the boundaries of the detected hot and cold regions are also presented.

at the centroid of the hot/cold regions at the same axial location,  $\bar{\phi}$ . The ensemble average of  $\phi/\bar{\phi}$  within these regions was then calculated for equally spaced bins of length  $0.25D$  in the axial direction. The binned data,  $\langle\phi_{reg}/\bar{\phi}\rangle$ , is presented in Figure 11 as a function of axial location for a series of particle Stokes numbers with  $\bar{\phi} = 1.4 \times 10^{-3}$  and  $\dot{Q}_0 = 2410$  W. The results show that the average measured particle volume fraction within the determined hot regions is significantly greater than both the mean and that measured within the cold regions, for each particle diameter distribution investigated. A value of  $\langle\phi_{reg}/\bar{\phi}\rangle > 3$  was measured in the region  $2.3 < x/D < 3.5$  for the case with  $Sk_D = 514$ , and  $\langle\phi_{reg}/\bar{\phi}\rangle > 1.5$  for  $Sk_D \leq 163$  throughout the region  $1.5 < x/D < 3.5$ . The high value at  $x/D = 2.375$  for  $Sk_D = 514$  is most likely an anomaly due to the combination of the low average temperature rise at this location and low particle number density for this case. The value of  $\langle\phi_{reg}/\bar{\phi}\rangle$  was found to be greater than unity in the hot regions for each  $Sk_D$  and for all  $x/D > 1.5$ . This implies that, in the region  $1.5 < x/D < 3.5$ , the hot regions are coherent and/or that the particles remain sufficiently hot for strong thermal gradients in the surrounding gas to be continually generated through convective heat transfer between the hot particles and gas. Conversely, within the cold regions, it can be seen that  $\langle\phi_{reg}/\bar{\phi}\rangle$  is generally less than 1, with  $\langle\phi_{reg}/\bar{\phi}\rangle \approx 0.5$  for all  $x/D$  for the case with  $Sk_D = 86$ . The correlation between the gas temperature and particle volume fraction decreases slightly with axial distance, in the region downstream from the end of the heating region ( $x/D > 1.5$ ). This suggests that mixing of the gas-phase becomes increasingly significant, relative to the convective heat transfer with the particles, as the flow moves downstream. While these measurements are limited to the near-field of the jet flow, it is expected that in the far-field these correlations will continue to weaken with axial distance.

Figure 12 presents  $T_g - T_a$  as a function of the local particle volume fraction measured within a radius of  $0.1D$  around each particle ( $\phi_{loc}$ ), normalised by the local time-averaged volume fraction  $\bar{\phi}$ , for a series of  $Sk_D$  with  $\bar{\phi} = 1.4 \times 10^{-3}$  and  $\dot{Q}_0 = 2410$  W (top) together with a series of axial distances with  $Sk_D = 86$ ,  $\bar{\phi} = 1.4 \times 10^{-3}$  and  $\dot{Q}_0 = 2410$  W (bottom). Three temperatures are presented for the three flow conditions, namely  $T_{g,Hi}$ ,  $T_{g,Lo}$  and  $T_{g,Vd}$ , as defined in Section 2.3. It should be noted that the local volume fraction within all voids is  $\phi_{loc} = 0$  by this definition. The value of  $\bar{\phi}$  is towards the lower end of the four-way coupling regime ( $10^{-3} < \phi < 100$ ), for which both particle-fluid and particle-particle interactions are significant. Data are only reported within the region of  $2 < x/D < 2.25$ ,  $|r/D| < 0.3$ , which is immediately downstream from the heating region where the temperature difference between the particles and gas is the greatest. Within this region, the radial profiles of the time-averaged temperature and particle

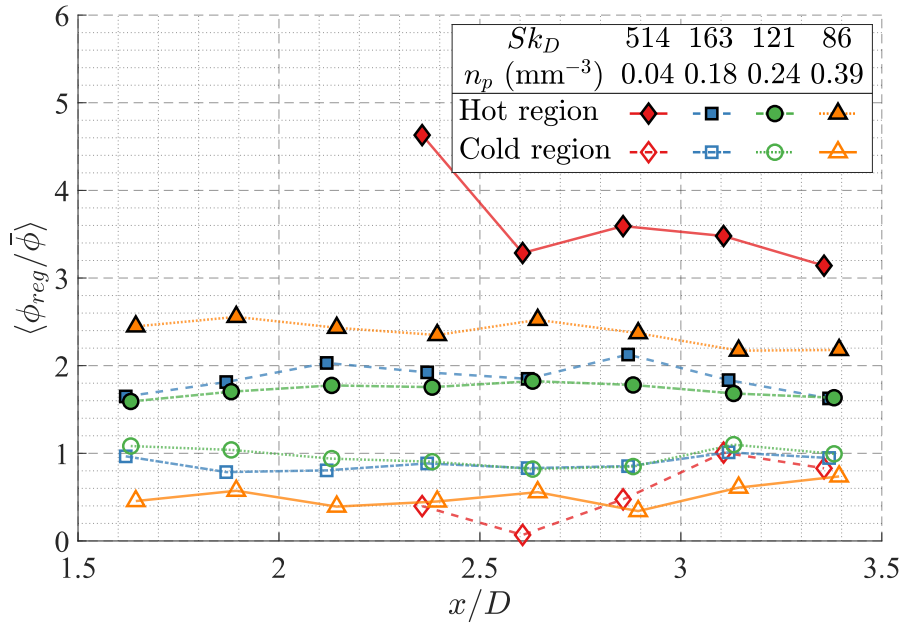


Figure 11: Ensemble average of the measured particle volume fraction within the detected hot and cold regions,  $\phi_{reg}$ , normalised by the time-averaged volume fraction at the same location,  $\bar{\phi}(x)$ , as a function of axial location for a series of  $Sk_D$  and with constant values of  $\bar{\phi} = 1.4 \times 10^{-3}$  and  $\dot{Q}_0 = 2410$  W.

volume fraction are also close to uniform, with the range of  $\bar{T}_g$  being less than 15 °C and with  $\phi$  being within 20% of the centreline value for each case [17]. Therefore, the non-uniformities in the particle volume fraction due to the radial distribution at the jet exit are small for this dataset. As such, the random variations in the local volume fraction are expected to be the primary driver for any gas-phase temperature variation.

The results show that the gas temperature is strongly correlated with the local particle volume fraction. The temperature difference in regions with  $\phi_{loc}/\bar{\phi} > 0$  is greater than that in regions with  $\phi_{loc}/\bar{\phi} = 0$  for all  $Sk_D$  and locations downstream from the heating beam. Furthermore,  $T_g$  also increases with an increase in  $\phi_{loc}/\bar{\phi}$  for each flow condition. For a given value of  $\phi_{loc}/\bar{\phi}$  the measured temperature around particles within clusters  $T_{g,Hi}$  is generally higher than  $T_{g,Lo}$ , implying that regions with clustering have higher local temperatures than the regions that do not. However, this difference is generally modest with  $T_{g,Hi} - T_{g,Lo} < 3$  °C, suggesting that the magnitude of local particle volume fraction has a greater influence on the temperature than the location of the clusters.

The results also show that the peak values of for  $\phi_{loc}/\bar{\phi}$  are higher in the regions around particles determined to be in clusters than in other regions, consistent with the definition of clusters being local regions of high volume fraction. Within the range of particle loadings and particle diameters investigated, the effect of  $\phi_{loc}$  on  $T_g - T_a$  is small compared to the effect of  $\bar{d}_p$ . For example, for  $Sk_D = 121$ ,  $T_{g,Hi} - T_a$  increases from 20 °C to 29 °C for a four-fold increase in the local volume fraction from  $\phi_{loc}/\bar{\phi} = 1$  to  $\phi_{loc}/\bar{\phi} = 4$ . However, for a decrease of the particle diameter by approximately half, from 423  $\mu\text{m}$  to 205  $\mu\text{m}$  (i.e., equivalent to an eight-fold increase in particle number density), but with a fixed volume fraction of  $\phi_{loc}/\bar{\phi} = 3$ , the value of  $T_{g,Hi} - T_a$  increases from 8 °C to 24 °C. The gradient of the increase in temperature with  $\phi_{loc}/\bar{\phi}$  (i.e. the slope of the lines in Figure 12, top) increases with  $\phi_{loc}/\bar{\phi}$ , for the cases with  $Sk_D \leq 121$  and  $\phi_{loc}/\bar{\phi} > 2.5$ . This slope can also be seen to increase with a decrease in  $Sk_D$  (i.e., a decrease in particle diameter). Together, these results imply that, for sufficiently small particle diameters, both the diameter and local volume fraction of particles in the flow impact significantly on the instantaneous gas-phase temperature distribution. Therefore, in flows where the local volume fractions can be significantly higher than the mean, such as in flows with aerodynamic particle clustering where  $\phi_{loc}/\bar{\phi} > 10$  has been measured [40], variations in the gas phase temperature can be expected to be particularly significant.

At the axial location upstream from the heating laser, for  $x/D = 0.75$ , all three temperatures  $T_{g,Hi}$ ,  $T_{g,Lo}$  and  $T_{g,Vd}$  are measured to be approximately zero regardless of the local particle volume fraction. This is as expected,

because the particles are yet to be heated directly at this point, although multiple scattering of the heating laser by particles may lead to a broadening of the heating region. However, with an increase in the axial distance downstream from the heating region ( $x/D > 0.9$ ), not only does the temperature rise increase, but the correlation between the local particle volume fraction and temperature rise also increases, as evidenced by the slope of the lines in Figure 12 (bottom). This increase in  $T_g$  with  $\phi_{loc}/\bar{\phi}$  downstream from the heating region implies that the flow is being heated continually by the particles throughout the measurement region. Additionally, the temperature around particles remains significantly greater than the temperature in the voids suggests that the heat transfer from particle-gas convection is dominant compared to the mixing and convection within the gas-phase, throughout the near-field. This, in turn, implies that the particle clusters retain strong coherence with time, or are relatively long-lived. Hence, the mechanisms that form particle clusters influence the local distributions of temperature.

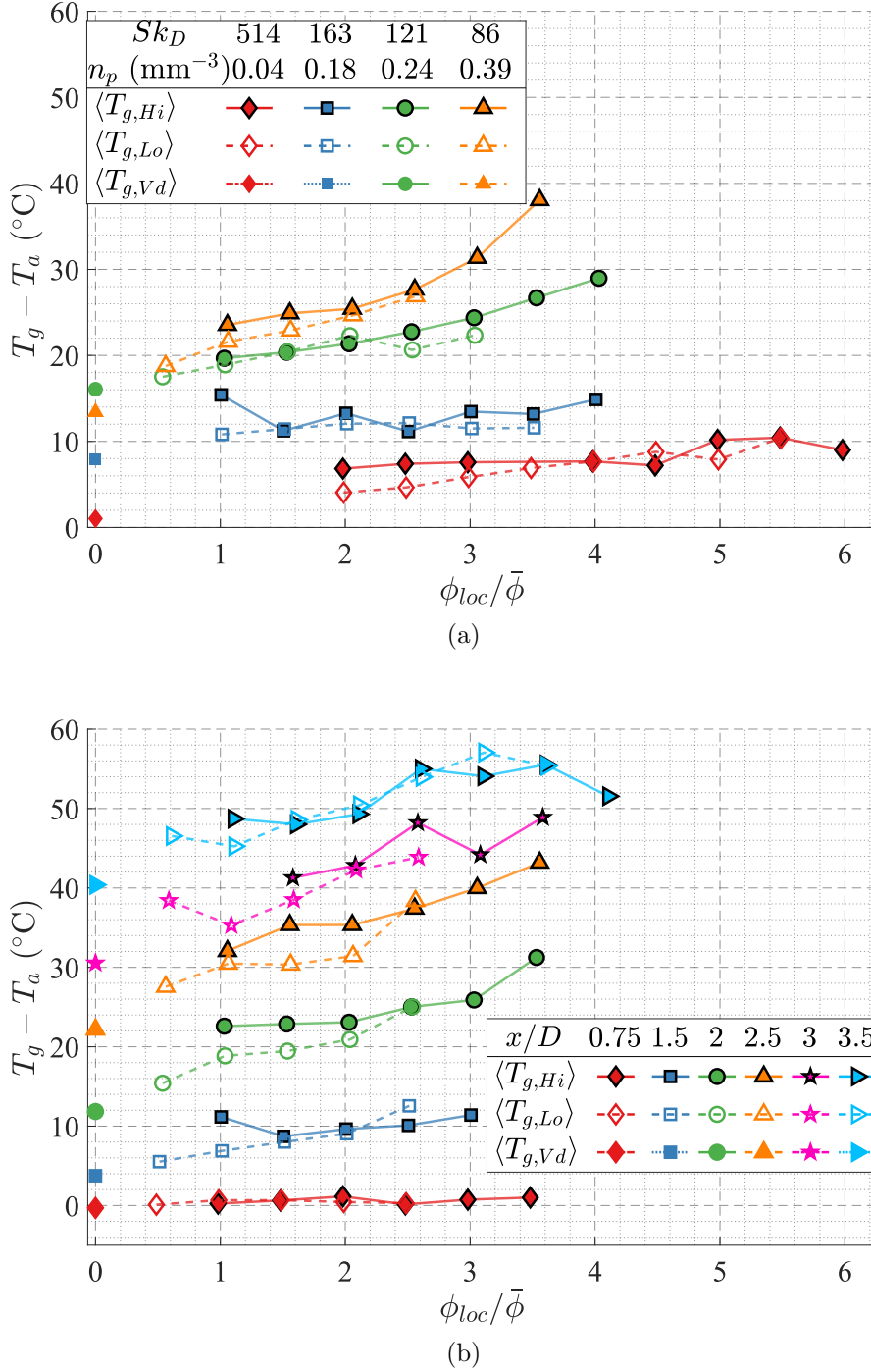


Figure 12: The ensemble average of the temperature above ambient as a function of the local particle volume fraction, for the regions around particles inside clusters, outside clusters and in voids, for a series of  $Sk_D$  with  $\bar{\phi} = 1.4 \times 10^{-3}$  and  $\dot{Q}_0 = 2410$  W measured in the region immediately downstream from the heating laser of  $2 < x/D < 2.25$  (a) and for a series of axial locations for the flow with  $Sk_D = 86$ ,  $\bar{\phi} = 1.4 \times 10^{-3}$  and  $\dot{Q}_0 = 2410$  W (b).

## 4 Conclusions

Detailed planar measurements within a radiatively heated particle-laden jet have shown that the instantaneous distributions of both the particle number density and the gas phase temperature are highly non-uniform and correlated, both spatially and temporally. Both the average gas-phase temperature and the range of temperatures measured were found to increase with axial distance downstream from the radiative heating region. Localised regions of high and low temperature were identified from the images of the gas-phase temperature following normalisation by the time-averaged value and smoothing at a suitable length scale, with the location of the ‘hot’ and ‘cold’ regions varying significantly both spatially and temporally. The hot regions were found to be more prevalent near to the jet centreline, while the cold regions were more prevalent near to the jet edge. These results are attributed to the particle loading at the jet exit being preferentially concentrated on the jet axis and the effect of cooling from the unheated co-flow. The local particle volume fraction within the hot regions was  $\phi_{reg}/\bar{\phi} > 1.5$  for all investigated cases, while  $\phi_{reg}/\bar{\phi} < 1$  was typical within the cold regions. This implies that the convective heat transfer between the hot particles and surrounding gas is faster than its rate of dissipation through the surrounding gases due to mixing and convection, at least within the measurement region and for the conditions investigated. These results were found to be consistent with axial distance, indicating that the regions with both high temperature and particle volume fraction remain coherent over the range  $0.3 < x/D < 3.7$ . Importantly, this implies that the particle clusters are relatively long-lived, so that the local distributions of temperature are influenced by the long history of large-scale flow features and cluster propagation.

Furthermore, the temperature in regions surrounding particles was found to be greater than that in the void regions downstream from the radiatively heated region, with the local gas-phase temperature increasing with an increase in the local particle volume fraction. Additionally, the temperature around particles within clusters was greater than those outside of clusters, although the temperature difference was relatively modest. The effect of the local particle volume fraction on the temperature rise was also found to increase with an increase in the particle number density.

For the conditions investigated, the measured proportion of particles in clusters, as calculated using Voronoi diagrams, closely matched that of a dataset simulated using a random particle distribution. The finding that they match a random distribution is consistent with all cases being evaluated in the high Stokes number regime. The particle distributions, both within and downstream from the radiative heating region, are independent of the

radiative flux. This implies that the effects of any thermal gradients on the particle-phase distributions (i.e., any buoyancy-induced effects) are negligible in the near field for these flows in the high Stokes number regime, even for fluxes up to 40 MW/m<sup>2</sup>.

## References

- [1] B. Klotz. “New developments in precalciners and preheaters”. In: *1997 IEEE/PCA Cement Industry Technical Conference. XXXIX Conference Record (Cat. No.97CH36076)*. 1997, pp. 255–280.
- [2] G. J. Nathan, P. A. M. Kalt, Z. T. Alwahabi, B. B. Dally, P. R. Medwell and Q. N. Chan. “Recent advances in the measurement of strongly radiating, turbulent reacting flows”. In: *Progress in Energy and Combustion Science* 38.1 (2011).
- [3] A. Williams, M. Pourkashanian and J. M. Jones. “Combustion of pulverised coal and biomass”. In: *Progress in Energy and Combustion Science* 27.6 (2001), pp. 587–610.
- [4] W. M. Fish. “Alumina calcination in the fluid-flash calciner”. In: *Essential Readings in Light Metals*. Vol. 1. Switzerland: Springer International Publishers, 2016, pp. 648–652.
- [5] J. A. H. Oates. *Lime and limestone : chemistry and technology, production and uses*. Weinheim, Germany: Wiley-Vch, 1998.
- [6] IEA. *Renewable Energy for Industry*. Report. IEA, 2017.
- [7] S. J. Davis et al. “Net-zero emissions energy systems”. In: *Science (American Association for the Advancement of Science)* 360.6396 (2018), eaas9793.
- [8] A. de Pee, D. Pinner, O. Roelofsen, K. Somers, E. Speelman and M. Witteveen. *Decarbonization of industrial sectors: the next frontier*. Report. McKinsey and Company, 2018.
- [9] E. T. Commission. *Making Mission Possible - Delivering a Net-Zero Economy*. Report 1.0. Energy Transitions Commission, 2020.
- [10] S. Balachandar and J. Eaton. “Turbulent Dispersed Multiphase Flow”. In: *Annual Review of Fluid Mechanics* 42 (2010), pp. 111–133.
- [11] H. Pouransari and A. Mani. “Effects of Preferential Concentration on Heat Transfer in Particle-Based Solar Receivers”. In: *Journal of Solar Energy Engineering* 139.2 (2016), pp. 021008–021008–11.

- [12] D. C. Ozcan, S. Brandani and H. Ahn. “A Hybrid Carbon Capture System of Indirect Calcination and Amine Absorption for a Cement Plant”. In: *Energy Procedia* 63 (2014), pp. 6428–6439.
- [13] C. K. Ho. “A review of high-temperature particle receivers for concentrating solar power”. In: *Special Issue: Solar Energy Research Institute for India and the United States (SERIUS) – Concentrated Solar Power* 109 (2016), pp. 958–969.
- [14] D. Davis, F. Muller, W. Saw, A. Steinfeld and G. Nathan. “Solar-driven alumina calcination for CO<sub>2</sub> mitigation and improved product quality”. In: *Green Chem.* 19.13 (2017), pp. 2992–3005.
- [15] A. Meier, E. Bonaldi, G. M. Cella, W. Lipinski and D. Wullemmin. “Solar chemical reactor technology for industrial production of lime”. In: *Solar Energy* 80.10 (2006), pp. 1355–1362.
- [16] N. Siegel, C. Ho, S. S. Khalsa and G. Kolb. “Development and Evaluation of a Prototype Solid Particle Receiver: On-Sun Testing and Model Validation”. In: *Journal Of Solar Energy Engineering-Transactions Of The Asme* 132.2 (2010).
- [17] E. W. Lewis, T. C. W. Lau, Z. Sun, Z. T. Alwahabi and G. J. Nathan. “Insights from a new method providing single-shot, planar measurement of gas-phase temperature in particle-laden flows under high-flux radiation”. In: *Experiments in Fluids* 62.4 (2021), p. 80.
- [18] A. J. Banko, L. Villafañe, J. H. Kim and J. K. Eaton. “Temperature statistics in a radiatively heated particle-laden turbulent square duct flow”. In: *International Journal of Heat and Fluid Flow* 84 (2020), p. 108618.
- [19] S. Elgobashi. “An Updated Classification Map of Particle-Laden Turbulent Flows”. In: *IUTAM Symposium on Computational Approaches to Multiphase Flow: Proceedings of an IUTAM Symposium held at Argonne National Laboratory, October 4–7, 2004*. Ed. by S. Balachandar and A. Prosperetti. Dordrecht: Springer Netherlands, 2006, pp. 3–10.
- [20] J. K. Eaton and J. R. Fessler. “Preferential concentration of particles by turbulence”. In: *International Journal of Multiphase Flow* 20 (1994), pp. 169–209.
- [21] J. R. Fessler, J. D. Kulick and J. K. Eaton. “Preferential concentration of heavy particles in a turbulent channel flow”. In: *Physics of Fluids* 6.11 (1994), pp. 3742–3749.

- [22] R. Monchaux, M. Bourgoïn and A. Cartellier. “Preferential concentration of heavy particles: A Voronoï analysis”. In: *Physics of Fluids* 22.10 (2010), p. 103304.
- [23] A. Frankel, H. Pouransari, F. Coletti and A. Mani. “Settling of heated particles in homogeneous turbulence”. In: *Journal of Fluid Mechanics* 792 (2016), pp. 869–893.
- [24] R. Zamansky, F. Coletti, M. Massot and A. Mani. “Radiation induces turbulence in particle-laden fluids”. In: *Physics of Fluids* 26.7 (2014), p. 071701.
- [25] N. Siegel, M. Gross and R. Coury. “The Development of Direct Absorption and Storage Media for Falling Particle Solar Central Receivers”. In: *Journal of Solar Energy Engineering* 137 (2015), p. 041003.
- [26] A. C. Eckbreth. *Laser diagnostics for combustion temperature and species*. 2nd ed. Combustion science and technology book series ; v. 3. Amsterdam: Gordon and Breach, 1996.
- [27] N. J. Kempema and M. B. Long. “Quantitative Rayleigh thermometry for high background scattering applications with structured laser illumination planar imaging”. In: *Applied Optics* 53.29 (2014), pp. 6688–6697.
- [28] A. Bohlin and C. J. Kliwer. “Communication: Two-dimensional gas-phase coherent anti-Stokes Raman spectroscopy (2D-CARS): Simultaneous planar imaging and multiplex spectroscopy in a single laser shot”. In: *The Journal of Chemical Physics* 138.22 (2013), p. 221101.
- [29] C. Schulz and V. Sick. “Tracer-LIF diagnostics: quantitative measurement of fuel concentration, temperature and fuel/air ratio in practical combustion systems”. In: *Progress in Energy and Combustion Science* 31.1 (2005), pp. 75–121.
- [30] J. Lakowicz. *Principles of Fluorescence Spectroscopy*. 3rd ed. New York: Springer, 2006.
- [31] P. A. M. Kalt, C. H. Birzer and G. J. Nathan. “Corrections to facilitate planar imaging of particle concentration in particle-laden flows using Mie scattering, Part 1: Collimated laser sheets”. In: *Applied Optics* 46.23 (2007), pp. 5823–5834.
- [32] M. Cundy, P. Trunk, A. Dreizler and V. Sick. “Gas-phase toluene LIF temperature imaging near surfaces at 10 kHz”. In: *Experiments in Fluids* 51.5 (2011), pp. 1169–1176.

- [33] M. Luong, R. Zhang, C. Schulz and V. Sick. “Toluene laser-induced fluorescence for in-cylinder temperature imaging in internal combustion engines”. In: *Applied Physics B* 91.3 (2008), p. 669.
- [34] E. W. Lewis, T. C. W. Lau, Z. Sun, Z. T. Alwahabi and G. J. Nathan. “Luminescence interference to two-colour toluene laser-induced fluorescence thermometry in a particle-laden flow”. In: *Experiments in Fluids* 61.4 (2020), p. 101.
- [35] M. Luong, W. Koban and C. Schulz. “Novel strategies for imaging temperature distribution using Toluene LIF”. In: *Journal of Physics: Conference Series* 45.1 (2006), p. 133.
- [36] E. W. Lewis, T. C. W. Lau, Z. Sun, Z. T. Alwahabi and G. J. Nathan. “The effect of particle size and volumetric loading on the gas temperature distributions in a particle-laden flow heated with high-flux radiation”. In: *Accepted by the International Journal of Heat and Mass Transfer* (2021).
- [37] T. C. W. Lau and G. J. Nathan. “The effect of Stokes number on particle velocity and concentration distributions in a well-characterised, turbulent, co-flowing two-phase jet”. In: *Journal of Fluid Mechanics* 809 (2016), pp. 72–110.
- [38] I. Gillandt, U. Fritsching and K. Bauckhage. “Measurement of phase interaction in dispersed gas/particle two-phase flow”. In: *International Journal of Multiphase Flow* 27.8 (2001), pp. 1313–1332.
- [39] Z. T. Alwahabi, K. C. Y. Kueh, G. J. Nathan and S. Cannon. “Novel solid-state solar thermal simulator supplying 30,000 suns by a fibre optical probe”. In: *Optics Express* 24.22 (2016), A1444–A1453.
- [40] T. C. W. Lau and G. J. Nathan. “A method for identifying and characterising particle clusters in a two-phase turbulent jet”. In: *International Journal of Multiphase Flow* 88 (2017), pp. 191–204.
- [41] J.-S. Ferenc and Z. Nédá. “On the size distribution of Poisson Voronoi cells”. In: *Physica A: Statistical Mechanics and its Applications* 385.2 (2007), pp. 518–526.
- [42] T. C. W. Lau, J. H. Frank and G. J. Nathan. “Resolving the three-dimensional structure of particles that are aerodynamically clustered by a turbulent flow”. In: *Physics of Fluids* 31.7 (2019), p. 071702.